HHS Public Access

Author manuscript

Cell Rep. Author manuscript; available in PMC 2025 April 25.

Published in final edited form as:

Cell Rep. 2021 April 27; 35(4): 109013. doi:10.1016/j.celrep.2021.109013.

Transcriptional control of DNA repair networks by CDK7 regulates sensitivity to radiation in MYC-driven medulloblastoma

Bethany Veo[1], **Etienne Danis**[1], **Angela Pierce**[1,2], **Dong Wang**[1], **Susan Fosmire**[1], **Kelly D. Sullivan**[3], **Molishree Joshi**[3], **Santosh Khanal**[3], **Nathan Dahl**[1,2], **Sana Karam**[4], **Natalie Serkova**[5], **Sujatha Venkataraman**[1,2], **Rajeev Vibhakar**[1,2,6,7,*]

[1]Department of Pediatrics, University of Colorado Anschutz Medical Campus, Aurora, CO, USA

[2]Morgan Adams Foundation Pediatric Brain Tumor Research Program, Children's, Hospital Colorado, Aurora, CO, USA

[3]University of Colorado Cancer Center, Aurora, CO, USA

[4]Department of Radiation Oncology, University of Colorado Denver, Aurora, CO, USA

[5]Department of Radiology, University of Colorado Denver, Aurora, CO, USA

[6]Department of Neurosurgery, University of Colorado Denver, Aurora, CO, USA

[7]Lead contact

SUMMARY

MYC-driven medulloblastoma is a major therapeutic challenge due to frequent metastasis and a poor 5-year survival rate. MYC gene amplification results in transcriptional dysregulation, proliferation, and survival of malignant cells. To identify therapeutic targets in MYC-amplified medulloblastoma, we employ a CRISPR-Cas9 essentiality screen targeting 1,140 genes. We identify CDK7 as a mediator of medulloblastoma tumorigenesis. Using chemical inhibitors and genetic depletion, we observe cessation of tumor growth in xenograft mouse models and increases in apoptosis. The results are attributed to repression of a core set of MYC-driven transcriptional programs mediating DNA repair. CDK7 inhibition alters RNA polymerase II (RNA Pol II) and MYC association at DNA repair genes. Blocking CDK7 activity sensitizes cells to ionizing radiation leading to accrual of DNA damage, extending survival and tumor latency in xenograft mouse models. Our studies establish the selective inhibition of MYC-driven medulloblastoma by CDK7 inhibition combined with radiation as a viable therapeutic strategy.

*Correspondence: rajeev.vibhakar@cuanschutz.edu.

AUTHOR CONTRIBUTIONS

R.V. and B.V. designed the study and wrote the manuscript. B.V. conducted the experiments, performed data analysis, and prepared figures. K.D.S., M.J., S. Khanal, and S.V. created and S.F. performed CRISPR-Cas9 screen (F1). E.D. performed ChIP sequencing data processing and alignments (F4). A.P. performed mouse injections. D.W. performed RNA-seq analysis and GSEA (F3,6). N.S. performed MRI analysis (F4,7). S. Karam performed animal radiotherapy (F7). Additional ChIP sequencing analysis and editorial review were provided by N.D.

SUPPLEMENTAL INFORMATION

Supplemental information can be found online at https://doi.org/10.1016/j.celrep.2021.109013.

DECLARATION OF INTERESTS

The authors declare no competing interests.

Graphical abstract

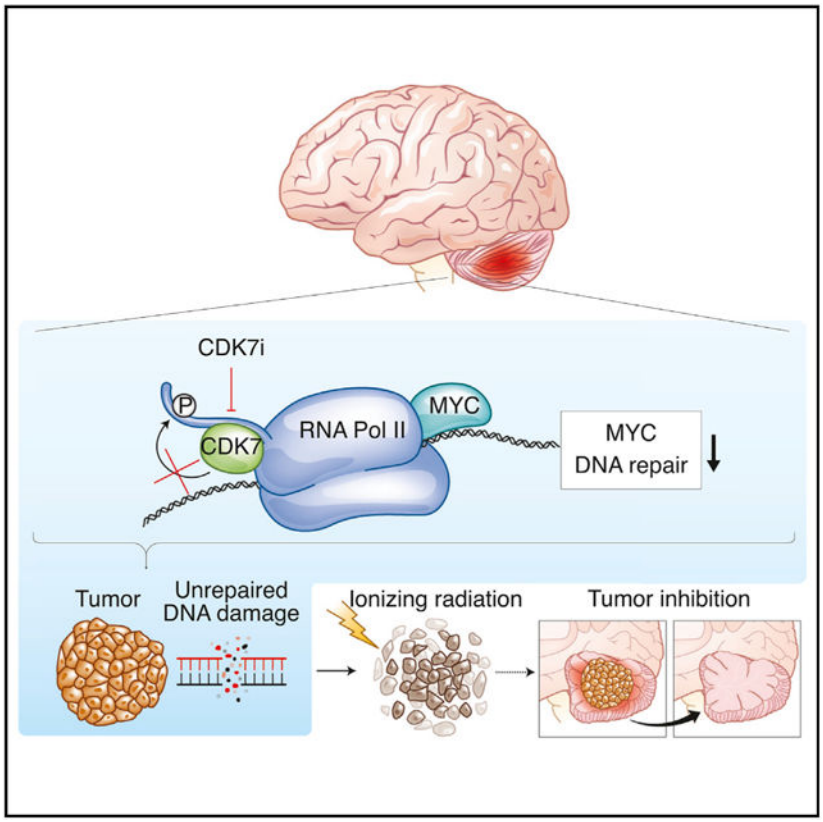

In brief

Veo et al. show chemical inhibition of CDK7 limits RNA Pol II and MYC presence at the TSS of core promoters mediating DNA repair. The selective transcriptional inhibition of DNA repair programs sensitizes MYC-amplified MB cells response to irradiation, providing maximal cell damage while reducing the effective radiation dose.

INTRODUCTION

Medulloblastoma (MB) is the most prevalent malignant brain tumor in children, accounting for 15%–20% of all pediatric brain tumors (Dhall, 2009). Therapeutic strategies for standard-risk patients consists of surgical resection followed by craniospinal irradiation and cytotoxic chemotherapy (Northcott et al., 2012a; Ramaswamy et al., 2016). This strategy has improved patient outcomes for standard-risk patients; however, high-risk patients still do poorly (Northcott et al., 2019; Ramaswamy et al., 2016). Previous molecular characterization of MB identified tremendous heterogeneity and categorically subdivided MB into 4 main subgroups (*WNT*, *SHH*, group 3, and group 4) with 12 subtypes (Schwalbe et al., 2017; Kool et al., 2012; Taylor et al., 2012; Cavalli et al., 2017a). Group 3 patients, and particularly group 3γ, represent a severe form of the disease with a poor 5-year survival rate of less than 30% (Cavalli et al., 2017b; Schwalbe et al., 2017). Group 3 tumors are associated with a higher incidence of metastatic disease and

are less responsive to the standard therapy, often leading to tumor relapse largely due to *MYC* gene amplification (Ramaswamy et al., 2016). MYC is a master transcription factor controlling regulatory circuitry for essential cellular processes including proliferation, stem cell self-renewal, metabolism, translation, and ribosomal biogenesis (Adhikary and Eilers, 2005; van Riggelen et al., 2010). In tumor cells, MYC functions as an oncogenic driver, creating a dependency on transcriptional regulation (Bradner et al., 2017; Kress et al., 2015). Pharmacologically targeting transcription factors including MYC remains challenging due to a lack of druggable pockets. Consequently, we sought to identify an alternative therapeutic target in MYC-driven MB using an unbiased CRISPR-Cas9 screen targeting the druggable genome. We identified the cyclin-dependent kinase 7 (CDK7) as a top mediator of MB growth. CDK7 is a major transcriptional regulator responsible for phosphorylating the carboxy-terminal domain (CTD) of the RNA polymerase II (RNA Pol II) subunit RPB1 on Ser5 (Fisher, 2018; Glover-Cutter et al., 2009; Chen et al., 2018; Core and Adelman, 2019).

In this study, we investigated the mechanisms of CDK7 regulatory function in MB growth and survival. We establish that genetic and chemical inhibition of CDK7 inhibits MB proliferation and enhances apoptotic mechanisms *in vitro* and in xenograft PDX models. Mechanistically, we demonstrate that chemical inhibition of CDK7 disrupts RNA Pol II and MYC association with a core set of genes mediating DNA repair. This action sensitizes MYC-amplified MB cells' response to irradiation, lowering the effective dose of radiation for maximal cell damage. We further observe that combined radiation and CDK7 chemical inhibition amplifies tumor latency in a xenograft tumor model, demonstrating the potential for pharmacological inhibition of CDK7 as a therapeutic strategy in MYC-amplified MB.

RESULTS

CDK7 is a critical dependency in MYC-amplified MB

In an effort to identify druggable targets in MYC-amplified MB, we performed a CRISPR-Cas9 screen targeting 1,140 genes for which there are, at present, drugs/chemical inhibitors or genes that contain druggable pockets based on *in silico* analysis (Figure S1A). Utilizing three MYC-amplified MB cell lines (D458, D425, and D341), we transduced cells and collected cell lysates before and 18 days after selection with puromycin (Figures 1A and 1B). Of the top strand guides found to be necessary for viability were genes that had previously been identified by us, including *WEE1*, *PLK1*, *BRD4*, and *EZH2* (Figure 1C) (Venkataraman et al., 2014; Harris et al., 2012, 2014; Alimova et al., 2012, 2013). Within this group of genes, we found *CDK7* expression to be similarly depleted (Figure 1D). While AURKA, CHEK1, WEE1, and PLK1 are notable therapeutic targets, the majority of CHEK1 and PLK1 inhibitors have been withdrawn or discontinued from clinical trials. We have recently demonstrated the efficacy of targeting WEE1 with AZD1775, and a clinical trial based on these data is under development at the Pediatric Brain Tumor Consortium (PBTC) (Moreira et al., 2020). We have also previously demonstrated that AURKA and CDK6 are targets in MB (El-Sheikh et al., 2010; Whiteway et al., 2013), and inhibitors are in phase 1 clinical trials for childhood brain tumors, making further investigation redundant. Thus, we chose to further focus on CDK7 because it is a novel component to MYC-amplified

MB. Further, the existing mechanistic rationale in transcriptionally amplified tumors and the availability of clinically significant chemical inhibitors makes it ideal for potential therapeutic development. CDK7 is a regulator of transcription initiation. As a part of the CDK-activating kinase (CAK) module in the TFIIH complex, CDK7 phosphorylates the Ser5 residue of RNA Pol II CTD. The phosphorylation of Ser5 enables promoter escape and proximal pausing of RNA Pol II within 20 to 120 nucleotides of the transcription start site (TSS). These steps prime RNA Pol II for recruitment of the positive transcription elongation factor b (P-TEFb), which facilitates release of RNA Pol II into productive transcriptional elongation (Chen et al., 2018; Larochelle et al., 2012).

To establish the relevant significance in patients, we investigated *CDK7* gene expression across 763 patient tumor samples. *CDK7* gene expression was associated with high levels of the *MYC* oncogene, displaying the highest expression across group 3 and, specifically, group 3γ MB, but was not genomically altered (Northcott et al., 2012b) (Figure 1E). Gene expression of *CDK7* and *MYC* positively correlated across group 3 and group 4 tumors (Figures S1B and S1C). Overall, patient survival in group 3 MB shows a survival advantage in tumors with lower levels of *CDK7* (Figure 1F). Additionally, we found higher CDK7 protein levels in high-MYC cell lines compared to low-MYC cells (Figure 1G). Similarly, concordant with the patient gene expression data, we observe more intense protein expression of CDK7 in group 3 tumor samples (Figure 1H). These results identify CDK7 as an important factor in the maintenance of MB growth and coordinate *CDK7* expression with MYC abundance in the most aggressive form of MB.

Genetic knockdown of CDK7 represses MB growth

To further determine the involvement of CDK7 in MB proliferation, we performed genetic depletion studies by knocking down *CDK7* with three independent short hairpin RNAs (shRNAs) in MYC-amplified cell lines D458 and D425. Reduction of CDK7 by 70%–80% was achieved with all three shRNAs (Figures 2A and 2B). Importantly, depletion of CDK7 decreased RNA Pol II Ser5 phosphorylation, on average, by 50%–30% (Figures 2A and 2B), whereas RNA Pol II Ser2 phosphorylation maintained similar levels or increased slightly.

MB is thought to include brain tumor stem cells, which promote proliferation, cancer stem cell self-renewal, and resistance to traditional therapeutic interventions (Singh et al., 2003). Following knockdown (KD) of CDK7, we assessed cell self-renewal and proliferation through a neurosphere growth assay in D458 and D425 cell lines. CDK7 depletion shows substantial inhibition of neurosphere growth as compared to the shNull in both D458 and D425 cells (Figure 2C). To further understand if neurospheres failed to grow initially or if self-renewal was disrupted, 10-day-old neurospheres were collected and re-plated as secondary spheres. Similarly, CDK7-depleted cells were unable to sustain growth, whereas shNull D458 and D425 neurospheres continued to grow and develop new neurospheres (Figure S2A). These data suggest that loss of CDK7 prevents further proliferation of MB cells and interrupts self-renewal. To then establish whether CDK7 loss impaired the ability of MB cells to form adhesion-independent colonies, we performed a methylcellulose assay. CDK7-depleted cell lines showed a 50% reduction in the number of colonies in D425 cells compared with controls, whereas in D458 cells, fewer than 50 colonies formed (Figures

2D and S2B). To determine whether the observed decrease in cell number was due to a cessation of growth or an increase in cell death, we examined Annexin V (+) by flow cytometry. D458 cells depleted of CDK7 showed a 40%–60% increase in Annexin V (+), suggesting that loss of CDK7 leads to an increase in apoptotic cells (Figures 2E and S2C). Likewise, D425 shCDK7 cells increased Annexin V (+) by 15%–25%. We further evaluated the transcriptomic profile of CDK7-depleted D458 cells. A complete cessation of gene expression was not observed (Figure S2E). Interestingly, gene set enrichment analysis (GSEA) identified an enrichment of apoptotic mechanisms as well as the deregulation of double-stranded break (DSB) repair and homologous DNA pairing (Figure S2F). These results show CDK7 is an essential component to MYC-amplified MB growth, and reduction of CDK7 disrupts MB propagation and self-renewal by enhancing apoptosis.

To evaluate whether CDK7 depletion effects tumor growth *in vivo*, we utilized bioluminescent CDK7 KD D458 and D425 cells for cerebellar injections into nude mice. Control mice formed large tumors by 24 days post-injection and were sacrificed due to tumor burden by 32 days post-injection (Figure 2F). In contrast, shCDK7-D458-injected mice had not formed visible tumors as detected by bioluminescence at 24 days post-injection (Figure 2F). Imaging of D458 shCDK7 mice was continued up to 75 days post-injection (Figure S2D). At the endpoint, a single mouse had succumbed to tumor burden by day 62, whereas all others remained healthy (Figure 2G). Similarly, D425 shNull mice developed tumors by day 10 and needed to be sacrificed by day 25 due to tumor burden. Delayed tumor formation was observed in 425 shCDK7 mice, where tumors were evident by day 23 (Figure 2F). Survival in D425 shCDK7 mice was enhanced by 10 days compared to shNull mice (Figure 2G). These *in vivo* results show reducing *CDK7* expression dramatically increased the time to tumor burden and, in the case of D458 cells, prevented tumor growth altogether in 5 of 6 mice. D425 cells carry a *P53* mutation in addition to *MYC* amplification, which may impact tumor survival. Taken together, the genetic depletion of *CDK7* confirms the results from the CRISPR-Cas9 druggable screen and establishes CDK7 as an essential factor mediating MYC-amplified MB growth.

CDK7 chemical inhibition displays potent selectivity to MYC-amplified MB

Several covalent inhibitors of CDK7 display promise as clinically relevant inhibitors and are currently in phase I clinical trial for advanced solid tumors. Among them, THZ1 and THZ2 show selectivity for CDK7 at 3.2 nM and 13.2 nM in *in vitro* kinase assays (Wang et al., 2015; Kwiatkowski et al., 2014). THZ2, derived from THZ1, maintains the specificity of THZ1 while increasing the half-life of the compound (Wang et al., 2015). Since THZ1 has been reported to target CDK12/13 at higher concentrations of >250 nM in *in vitro* kinase assays (Kwiatkowski et al., 2014), we also tested two additional CDK7 inhibitors, CT7001 and YKL-5–124 (Olson et al., 2019; Patel et al., 2018). To determine if group 3 MB cell lines were susceptible to THZ1 and THZ2 inhibition, we treated MYC-amplified cell lines D458 and D425 in addition to non-MYC-amplified cell lines ONS76 and UW228. In MYC-amplified cells D458 and D425, THZ1 showed considerable potency, with an IC_{50} of 10 nM (Figure 3A). UW228 and ONS76 cell lines, which represent SHH-type tumors, displayed a 10- and 20-fold increase in IC_{50} at 150 and 270 nM, respectively (Figure 3A). THZ2 also displays potent inhibition of D458 and D425 cells in comparison to non-MYC-amplified

cells (Figures 3A and S3A). Additionally, CT7001 and YKL-5–124 suppressed D458 and D425 cell viability at 4 nM and 36 nM for CT7001 and at 15 nM and 60 nM for YKL-5–124 (Figure S3B).

We further explored whether the presence of MYC enhanced the response to CDK7 chemical inhibition. We used an isogenic pair of ONS76 cell lines with doxycycline-inducible *MYC* overexpression or cells expressing an RFP control vector. ONS76-MYC cells exhibited a lower IC_{50} compared to ONS76-RFP control cells (Figures 3A and S3A). Likewise using non-transformed retinal pigment epithelial (RPE) cells, we found that the presence of MYC (RPE-MYC) enhanced the susceptibility to CDK7 chemical inhibition compared to cells expressing a neomycin control vector (RPE-Neo) (Figure S3A). To assess the impact of CDK7 inhibition on non-transformed cells, we treated normal human astrocytes (NHAs) and murine fibroblasts (NIH 3T3) with THZ1 and THZ2. NHA cells displayed IC_{50}s 40× higher than D458 cells when exposed to THZ1 and THZ2. NIH 3T3 cells exhibited 70× greater IC_{50} with THZ1 and 20× greater with THZ2 (Figure S3A). These results suggest that effective CDK7 inhibition and consequential chemical toxicity are enhanced in cells transformed by MYC. Additional tumors that exhibit MYC transcriptional addiction are reported to respond to THZ1, albeit at higher concentrations than we have found (Lu et al., 2019; Nagaraja et al., 2017; Wang et al., 2015; Christensen et al., 2014).

In order to determine if the MYC-amplified MB cells' response to THZ1 recapitulates genetic depletion of *CDK7*, we first examined MB cell propagation as neurospheres. Higher concentrations ranging from 2 μM to 50 nM completely inhibited neurosphere growth over the 10-day period, whereas minimal growth was observed at 10-nM THZ1 (Figure S3C). Compared with DMSO, the striking inhibition of neurosphere proliferation with THZ1 mimics the genetic KD of *CDK7* observed previously. We then evaluated independent colony formation of D458 and D425 cell lines exposed to THZ1 at IC_{20}, IC_{30}, and IC_{50}. A limited number of colonies formed at 2 nM in the D458 cell line; however, 7- and 10-nM concentrations significantly reduced colonies from both D458 and D425 cells (Figure 3B). These results recapitulate our genetic KD study and show that THZ1 effectively inhibits independent colony growth as well as neurosphere growth.

We then evaluated the dependency of THZ1 on increased MYC expression. High-*MYC*-expressing MB cells (D458 and D425) as well as ONS76-RFP and ONS76-MYC were exposed to 50 nM THZ1 and THZ2 for 48 h. Treatment reduced Ser5 phosphorylation by ≥40% in D458 and D425 cells in addition to the ONS76-MYC cells (Figures 3C, S3D, and S3E). THZ1 and THZ2 treatment had a minimal effect on Ser2 phosphorylation in all cell lines, similar to CDK7 genetic KD. (Figures 3C, S3D, and S3E). Additionally, we observed little change in CDK7 or CDK9 protein levels with treatment (Figures 3C, S3D, and S3E).

To test if treatment with THZ1 and THZ2 induces cell death, we evaluated cleavage of PARP. In D458 and D425 cells, we observed a 2-fold increase in cleaved PARP (Figures 3C and S3D). ONS76-MYC and ONS76-RFP cells display some induction of cleaved PARP as well (Figures 3C and S3E). These results suggest THZ1 and THZ2 induce apoptosis. Separately, we examined D458 and D425 cells' response to CT7001 and YKL-5–124 at 50 nM for 48 h. Depletion of RNA Pol II Ser5 was evident in CT7001-treated cells and

muted in YKL-5–124 cells, mirroring prior experiments with YKL-5–124 that show no effect on RNA Pol II phosphorylation (Olson et al., 2019). However, minor PARP cleavage was detected in both treatments by western blot (Figure S4A). Since THZ1 and THZ2 treatment disrupts MYC-transcriptional dependencies, we examined if MYC protein levels were altered by treatment. In D458 and D425 cells, a reduced level of MYC by 50% is observed with THZ1 and is more prominent with THZ2 treatment at 60%–68% (Figures 3C and S3D). These data suggest that CDK7 alters MYC expression in addition to potentiating MYC-driven transcription. Though the ONS76-RFP cell line has lower levels of MYC protein, we did not find any change with THZ1 or THZ2 treatment. However, when we ectopically induce MYC expression in ONS76 cells, they become sensitive to THZ1 and THZ2 treatments, which decrease MYC protein by 40% in these cells (Figures 3C and S3E). Once more, NHA and NIH 3T3 cells exposed to 50 nM THZ1 and THZ2 displayed no measurable effects to RNA Pol II Ser5 phosphorylation or PARP (Figures S3F and S3G). Altogether, these results suggest THZ1 and THZ2 prevent CDK7 catalytic activity, limiting RNA Pol II Ser5 phosphorylation in the context of MYC expression.

To fully understand the transcriptional response to THZ1 treatment in group 3 MB cells, we performed an RNA sequencing (RNA-seq)-based global gene expression analysis on D458 cells treated with THZ1 at IC_{50} for 48 h. Significant differential gene expression was set at $p < 0.05$ and shows 40% of genes decreased expression (Figure 3D). GSEA broadly shows the depletion of MYC transcriptional targets (Figure 3E). Gene Ontology (GO) analysis performed on the downregulated genes shows a significant association with DNA repair, DSB repair, termination of transcription, and replication (Figure 3F), whereas upregulated genes associated with translation initiation and mRNA catabolism (Figure 3G). Previous examination of THZ1 treatment in neuroblastoma does not report significant association of CDK7 inhibition with DNA repair (Chipumuro et al., 2014). We reanalyzed the previously reported microarray data from THZ1-treated MYCN-amplified Kelly cells (Figures S3H and S3I) and non-MYCN-amplified SH-SY5Y cells (Figure S3J). We found that CDK7 inhibition by THZ1 deregulates DNA repair networks in MYCN-amplified cells, confirming our own results. Thus, global gene expression analysis indicates that even at 10-nM THZ1, group 3 MB cells respond dramatically to CDK7 inhibition by abrogating the effect of MYC and inducing cell death mechanisms, recapitulating the transcriptomic profile of CDK7 genetic depletion.

CDK7 inhibitor effects in orthotopic and patient-derived xenograft mouse models of MB

To determine the relative potency of CDK7 chemical inhibition *in vivo*, we tested THZ2 treatment in orthotopic mouse models of MB growth. We elected to use THZ2 due to the enhanced half-life of THZ2 *in vivo* (Wang et al., 2015). Bioluminescent D458 or D425 cells were injected into murine cerebellum to generate orthotopic xenografts. Intraperitoneal injections of THZ2 at 15 mg/kg or vehicle were then conducted daily for 25 days. D458 orthotopic mice exposed to vehicle displayed tumor growth consistent with our previous reports showing the first signs of tumor ranging from days 10 to 12 (Figure 4A) (Veo et al., 2019). Initial IVIS signals showed similar tumor sizes among all cohorts; however, tumor growth continued to slow in THZ2-treated mice, significantly reducing the average IVIS signal (Figure 4B). All vehicle-treated mice had extensive tumor burden 30 days

post-injection and had to be euthanized, whereas 5 of the 6 D458 THZ2-treated cohort were still alive at the same time point (Figure 4F). THZ2-treated D458 mice survived, on average, 2.5 days longer compared to vehicle-treated mice (Figure 4F). Similarly, D425 orthotopic mice treated with vehicle displayed progressive tumor growth (Figures 4C and 4D). The D425 cell line grows more aggressively, and initial tumors were first identified by IVIS on day 8 post-injection, whereas 7 of 9 vehicle-treated mice succumbed to tumor burden and euthanasia by day 28 (Figure 4F). The D425 THZ2-treated cohort displayed slowed progression of tumor growth by IVIS, with 5 of 9 still alive at the same time point (Figures 4D and 4F). Survival in D425 THZ2-treated mice was extended by 3 days (Figure 4F).

MRIs were performed on two mice from vehicle- and THZ2-treated cohorts from D458 and D425 mice to examine tumor volumes and brain morphology. The average tumor volume from THZ2-treated cohorts was smaller in both models, agreeing with IVIS imaging (Figure 4E). Additionally, vehicle-treated cohorts exhibited edema and tumor invasiveness into the ventricular space 1 week earlier than did THZ2-treated mice (Figure S4C).

The efficacy of THZ2 in MB cell line orthotopic xenografts instigated more direct studies using the patient-derived xenograft, MED411FH (PDX411) (Cook Sangar et al., 2017). Mice began treatment with THZ2 at 15 mg/kg daily for 25 days with bi-monthly MRIs to monitor tumor size. MRIs of the vehicle-treated mice displayed early signs of edema and visible tumor in the ventricular space at 42 days (Figure S4C). In contrast, within the first 15 days of THZ2 treatment, PDX411 mice displayed reduced tumor volumes by MRI (Figure 4G). Tumor progression maintained a slower overall course in the THZ2-treated cohort, with 4 of 6 mice still alive on day 68, whereas 4 of 5 vehicle-treated mice had succumbed to tumor burden and were euthanized. The THZ2-treated cohort survived, on average, 13.5 days longer than the vehicle-treated cohort (Figure 4F). Although all xenograft mice eventually succumbed to tumor burden, we speculate that a non-optimized drug penetrance may have led to tumor expansion and/or resistant colony regrowth. Altogether, these results identify a statistically significant survival benefit in D458 and D425 xenografts, suggesting THZ2 treatments inhibit tumor growth.

Immunohistochemistry (IHC) was performed on collected mouse tissue at endpoints from each individual cohort. We found that expression of the proliferation marker Ki67 was reduced by 31% in THZ2-treated PDX411 tumors ($p < 0.0001$) and by 15% in THZ2-treated D425 tumors ($p < 0.05$) compared to vehicle-treated tumors (Figures 4H and 4I). To determine if THZ2 increased DNA damage within the tumors *in vivo*, we performed IHC for P-γH2AX. THZ2-treated tumors increased γH2AX staining by 12% in D425 tumors and by 4% in D458 and PDX411 tumors compared to vehicle-treated tumors (Figures 4H and 4I). Importantly, DNA damage was limited to tumors and not found in regions of neurogenesis, specifically the hippocampus (Figure S4D). We then evaluated the presence of cleaved caspase-3 to identify apoptotic tumor cells. THZ2-treated mice increased cleaved caspase-3 expression by 16% in D458 tumors ($p < 0.01$) and 12% in D425 tumors ($p < 0.05$) (Figures 4H and 4I). Likewise, activated caspase-3 was not found in the surrounding brain or hippocampus (Figure S4D).

To confirm that chemical toxicity did not produce adverse side effects in mice, blood samples were collected from mice at endpoint. Total white blood cell counts, lymphocytes, and neutrophils showed no significant differences between vehicle- and THZ2-treated mice with D458 and PDX411 xenografts (Figure S4E). Similarly, there were no significant changes in platelet and hemoglobin counts with THZ2 treatment compared with vehicle in D458 and PDX411 xenograft-bearing mice (Figure S4E). D425 mouse experiments were completed prior to beginning CBC collections. These results indicate THZ2 inhibition of CDK7 reduces tumor proliferation and increases apoptosis *in vivo*, while minimizing adverse neurological and systemic side effects.

CDK7 inhibition decreases RNA Pol II and MYC association on a subset of genes

To examine the mechanisms of CDK7 activity in MYC MB, we evaluated MYC and RNA Pol II promoter occupancy with and without CDK7 inhibition. We performed chromatin immunoprecipitation (ChIP) sequencing analysis using RNA Pol II and MYC antibodies in D458 cells that were treated with 10 nM THZ1. We found the disruption of CDK7 activity attenuates RNA Pol II density at or near the TSS in a subset of genes (Figure 5A). Importantly, sweeping decreases in global RNA Pol II poised transcription were not observed. Rather, we identified three gene clusters of differential RNA Pol II density. Cluster 3 demonstrates genes not transcriptionally active regardless of CDK7 activity. Cluster 2 indicates retention of Pol II binding on genes mediating mRNA processing and translation, as well as ribosome biogenesis (Figures 5A and S5A). Cluster 1 displays the most dramatic decrease in RNA Pol II density at the TSS. GO analysis identified genes primarily associated with DNA repair, DNA replication, and ncRNA processing (Figure 5B). ChIP sequencing of MYC shows decreased association of MYC at the TSS with CDK7 inhibition, in line with our transcriptomic analysis (Figure 5A). Clustering of MYC ChIP profiles identified select areas of decreased density at the TSS rather than a widespread decrease in promoter association (Figure 5A). Clusters 2 and 3 exhibit little change in MYC peak density, displaying regions of continued MYC transcriptional activity including translation and RNA catabolic processing and regions of transcriptional inactivity (Figures 5A and S5B). Depleted MYC promoter association was most prominent in cluster 1, with DNA repair processes topping the functional ontology list (Figure 5C). Further examination of the top genes in the DNA repair pathway of cluster 1 shows the association of RNA Pol II and MYC was significantly decreased at the TSS of genes mediating HR, including *BRCA2*, *BRCC3*, *RAD51c*, and *XRCC2* (Figure 5D). Conversely, the top genes in mRNA processing of cluster 2 have similar overall density for both RNA Pol II and MYC (Figure 5E). These results emphasize that inhibition of CDK7 activity diminishes RNA Pol II and MYC association at specific gene clusters. Further, the functional overlap between RNA Pol II and MYC produces a concerted transcriptional decline at genes promoting DNA repair.

Inhibition of CDK7 compromises homologous recombination and sensitizes MB cells to ionizing radiation

Transcriptional gene expression analysis revealed downregulation of genes mediating DNA repair and homologous recombination in addition to positive enrichment of genes responsible for apoptosis (Figures 6A and S6A). Volcano plots of homologous recombination and DNA repair gene sets show individual genes involved in homologous

recombination such as *BRCA2*, *RAD51*, and *RAD50* are decreased upon THZ1 treatment (Figure 6B). Likewise, GO analysis showed that within the downregulated gene set, the top genes affected were involved in DNA repair and homologous recombination (Figure 3F). We evaluated BRCA2 and RAD51 gene expression by qRT-PCR in shCDK7 KD cell lines and observed a significant decrease in expression (Figure S2G). To further validate if treatment with THZ1 reduced RNA Pol II association at individual promoters of genes involved in homologous recombination, we examined the promoters of *BRCA2*, *RAD51c*, a *RAD51* paralog, and *RAD51*. RNA Pol II peak density is noticeably depleted on *BRCA2* and *RAD51c* promoters (Figure 6C). Examining the *RAD51* promoter, we found RNA Pol II is localized to a region 10 kb upstream of the TSS demarcated by H3K27ac, suggesting the presence of an enhancer. With THZ1 treatment, RNA Pol II peaks are substantially reduced in this location (Figure S6B). *BRCA2* and *RAD51* are known targets of MYC; thus, MYC occupancy was also examined. Correspondingly, MYC peak density was reduced upon THZ1 treatment on the *BRCA2* promoter, *RAD51c*, and *RAD51* promoters, further validating our ChIP sequencing results (Figures 6C and S6B).

The disruption of repair mechanisms would impair tumor cells' defense mechanisms against commonly used therapeutic strategies such as ionizing radiation (IR). We found that THZ1 treatment reduced RNA Pol II density at promoters of these specific genes, thus showing that CDK7 chemical inhibition may sensitize MYC-amplified cells to DNA damage by preventing transcriptional amplification of DNA damage responders. To determine if MYC-amplified cells were more susceptible to IR after THZ1 treatment, D458 and D425 cells were exposed to THZ1 IC_{20} and increasing dosages of radiation (0, 2, 4, 6, 8, 10 Gy). Initial immunofluorescence staining for γH2AX at 4 h shows an accumulation of DNA DSBs in DMSO- and THZ1-treated cells exposed to 6 Gy compared to 0 Gy for control (Figure 6D). However, at 24 h post-radiation, THZ1-treated cells maintain a significantly higher level of DNA DSBs compared to DMSO, indicating a deficiency in DNA repair mechanisms (Figure 6D). To further assess the disruption of homologous recombination, we performed immunofluorescence of RAD51 and RPA1 in D458 cells treated with IC_{20} THZ1 and irradiated at 4 Gy. Consistent with decreasing HR function, a noticeable decrease in RPA1 and RAD51 foci was observed with THZ1 treatment (Figure S6D). Separately, treatment with CT7001 and YKL-5–124 also induced DNA DSBs in D425 cells, further affirming CDK7 inhibition effects DNA repair (Figure S6E).

We then examined induction of apoptosis by Annexin V staining of IR-exposed and THZ1-treated D458 cells. Exposure to THZ1 along with 2 or 6 Gy increased Annexin V (+) by >10% compared with DMSO, suggesting increased sensitivity to IR with THZ1 treatment (Figures 6E and S6C). The sensitivity enhancement ratio (SER) was then evaluated to determine the dosage of radiation with and without THZ1 or THZ2. In comparison to DMSO, D458 and D425 cells exposed to 200 pM (10-fold less the IC_{20}) THZ1 or THZ2 reduced the level of radiation needed to prevent independent colony growth. In D458 cells, a 2-Gy radiation dose results in a survival fraction of 0.47, and with THZ1 or THZ2 treatment, the survival fraction is reduced to 0.28 (THZ2) and 0.18 (THZ1) (Figure 6F). Similarly, in D425 cells, survival after exposure to 2-Gy radiation dose was 0.67, and with the addition of THZ1 treatment, survival reduced to 0.24 (Figure 6F). In order to achieve similar decreases in survival without drug treatment, the radiation dose would need to increase to 4 Gy in both

cell lines. At 50% survival, the SER scores for THZ1 of 1.61 and THZ2 of 1.04 in D458 and 2.49 and 1.88 in D425 signify a synergy between THZ1 or THZ2 treatment and radiation exposure (Figure 6F).

In vivo THZ2 treatment augments radiation sensitivity in group 3 MB cells

Given the observation that CDK7 inhibition sensitizes cells to IR, we sought to evaluate whether the combination of THZ2 and IR could be applied to the D458 orthotopic mouse model. Visible tumors were identified by IVIS imaging on day 11 post-injection (Figure 7A). Following tumor verification, mice were irradiated at 1.5 Gy for 5 days, and concurrent THZ2 treatment at 15 mg/kg or vehicle was initiated. Tumors showed visible reduction in IVIS signals 11 days after radiation (Figures 7A and 7C). In the irradiated vehicle-treated cohort, tumors recurred by week 2, and at 65 days post-injection, 8 of 9 mice developed extensive tumor burden requiring euthanasia. THZ2-treated mice delayed tumor recurrence with little to no tumor signal up to 3 weeks after exposure (Figures 7A and 7C), with 5 of 10 mice still alive 65 days post-injection. MRIs confirmed the presence of tumor growth in the vehicle-treated cohort in comparison to THZ2-treated mice (Figure 7B). The survival curve indicates a significant survival enhancement in THZ2-treated mice, where 2 mice failed to form tumors (Figure 7D). Overall, these results suggest THZ2 can extend the latency of tumor growth beyond treatment with radiation alone and may be an effective treatment for combination therapy.

DISCUSSION

Group 3 MB is largely devoid of driver mutations that can be therapeutically targeted; rather, the subgroup population is most commonly linked with *MYC* amplification (Ramaswamy et al., 2016; Northcott et al., 2012a). Amplification of *MYC* in MB is associated with poorer clinical outcomes, where tumors have a higher incidence of metastasis and recurrence (Northcott et al., 2012a). These high-risk tumors are more aggressive in nature and less responsive to standard chemotherapy and radiation interventions. Standard therapy for average-risk patients includes cranio-spinal radiation. However, high-risk patients still have no known optimal treatment. Significant neurocognitive impairment predominates in high-risk patients and young children, where experiences with long-term declines in IQ and memory are common due to ongoing nervous system development (Northcott et al., 2019; Ramaswamy et al., 2016). In a study that examined lowering the dosage of radiation to the posterior fossa, the results showed worsening patient outcomes; thus, radiation exposure remains unchanged (Kann et al., 2016).

The genomic amplification of *MYC* causes widespread transcriptional dysregulation of specific gene clusters that aid in tumor cell propagation and evasion of cell death mechanisms (Bradner et al., 2017) (Figure 7E). In MYC-amplified tumors, transcriptional amplification elevates replication stress, inducing responses to DNA damage. However, compensatory mechanisms sensed by ATR/CHK1 are also amplified by MYC, alleviating cellular stress and enabling further tumor propagation (Campaner and Amati, 2012). This process imparts the ability to evade DNA damaging therapeutics and IR, leading to recurrent tumors and metastatic disease (Ryan et al., 2012) (Figure 7E). While specifically targeting

MYC amplification has remained problematic due to the absence of druggable catalytic domains, the potential to indirectly target MYC has shown promise (Bradner et al., 2017). Here, we utilized a genome-wide loss-of-function CRISPR-Cas9 screen to identify specific targets in MYC-amplified MB that have a pre-validated chemical inhibitor. CDK7 was found to mediate MB growth in addition to protecting cells from apoptotic mechanisms.

Chemical inhibition of CDK7 has shown promise in multiple solid tumors that display hyper-active transcriptional dysregulation due to oncogene amplification (Nagaraja et al., 2017; Wang et al., 2015; Christensen et al., 2014; Chipumuro et al., 2014). Evidence of CDK7 inhibition selectivity is found in TNBC, which necessitates continuous active transcription compared to ER/PR+ breast cancers that contain the traditionally targeted genetic alterations (Wang et al., 2015). Similarly, in neuroblastoma and SCLC, CDK7 inhibition deregulates transcription of MYC and MYCN targets through super-enhancers, where non-MYCN-amplified tumors display minimal deregulation (Chipumuro et al., 2014). Further, transcriptionally amplified *GLI2* and *MYCN* SHH MB cell lines have shown susceptibility to CDK7 inhibition (Liu et al., 2019), in contrast to results with UW228 and ONS76, which are non- *MYCN*-, *GLI1*-, or *GLI2*-amplified SHH cells (Higdon et al., 2017; Swartling et al., 2010). We have found that CDK7 inactivation diminishes MYC and RNA Pol II at the TSS of confined gene clusters, compromising MYC transcriptional targets including *MYC* itself, DNA repair, ncRNA metabolism, and cell division networks (Figures 7E and S6B). Of further interest to our findings is the evidence of MYC directly altering RNA Pol II processive transcriptional elongation by recruiting SPT5 to promoters. The recruitment of SPT5 and transfer from MYC to RNA Pol II is mediated by CDK7 phosphorylation of Ser5 and displacement of TFIIE (Baluapuri et al., 2019). These MYC-induced actions enhanced RNA Pol II's processive transcriptional elongation rate—importantly, on the distal regions of MYC target genes. Thus, the identification of CDK7 in group 3 MB represents an opportunity to indirectly disrupt MYC transcriptional programs.

The systematic actions of TFIIH are necessary for global transcription; however, inhibition of the catalytic activity of CDK7 alone does not result in a genome-wide transcriptional blockade (Kanin et al., 2007; Glover-Cutter et al., 2009; Serizawa et al., 1993). To this end, previous studies with THZ1 and CDK7 inhibition have found broad transcriptional deregulation in tumors with hyper-transcriptional amplification using concentrations higher than 100 nM of THZ1(Chipumuro et al., 2014; Kwiatkowski et al., 2014; Liu et al., 2019). Off-target selectivity with larger concentrations may have contributed to the widespread inhibition of gene expression, where inhibition of CDK12/13 at 250–893 nM has been shown to reduce Ser2 and Ser5 phosphorylation of RNA Pol II (Olson et al., 2019; Kwiatkowski et al., 2014; Chipumuro et al., 2014; Dubbury et al., 2018). Notably, evidence of CDK12 inhibition inducing an elongation defect, leading to premature cleavage and polyadenylation of long DDR genes (Krajewska et al., 2019; Dubbury et al., 2018), demonstrates that CDK12 acting on elongation and CDK7 acting at initiation show functional continuity on highly transcribed genes. Additionally, reports of CDK7 directly activating CDK9, CDK12, and CDK13 suggest that complete decoupling of CDK7 activity from CDK12/13 may be difficult (Rimel et al., 2020; Larochelle et al., 2012). However, we found that CDK7 inhibition at 10 nM, well below the 250–893-nM range reported to inhibit

CDK12, disrupts DNA repair mechanisms, and the contribution from other kinases cannot be excluded.

Our data establish that with CDK7 genetic KD, the significant depletion of BRCA2 and RAD51 expression occurs. Furthermore, the shCDK7 transcriptomic profile mirrors THZ1-treated cells, where RNA-seq GSEA profiles show decreased enrichment of homologous recombination and DNA-repair-associated genes, supporting the idea that inhibition of CDK7 specifically deregulates MB tumor cells' defense mechanisms. We observed that decreased transcriptional amplification for *BRCA2*, *RAD51C*, and *RAD51* impacted the level of IR needed to induce cell death. Exposure to increased radiation and 10-fold-lower dosage of THZ1 or THZ2 enhanced the sustained presence of DSBs, indicating MB cells were more sensitive to radiation and less able to recover radiation-induced DNA damage. Without CDK7 blockade, cells are able to respond to the induction of DNA damage breaks, essentially limiting the effectiveness of IR on tumor cells. While MYC is known to transcriptionally target several DNA repair genes including *BRCA2* and *RAD51*, the downregulation of homologous recombination genes may be further exacerbated by CDK7s' activity as a CAK mediating CDK1/2 and role in the cell cycle (Larochelle et al., 2007). CDK1 is required for DSB-induced homologous recombination throughout the cell cycle and recruitment of RPA and RAD51(Ira et al., 2004). In support of this, another CDK7 inhibitor, YKL-5–124, was recently found to induce replication stress in SCLC cells independently of RNA Pol II CTD phosphorylation, blocking MCM2 at replication foci and inducing DNA damage and genomic instability (Zhang et al., 2020). Our testing of YKL-5–124 also displayed accumulation of P-γH2AX foci, demonstrating that inhibiting CDK7's activity as a CAK further enhances DNA damage. Overall, inhibition of CDK7 disadvantages MYC transcriptional programs in MB by collectively diminishing RNA Pol II and MYC association prominently at the TSS of genes mediating DNA repair and homologous recombination.

Importantly, our data, along with other recent reports, demonstrate a mechanism to drug MYC transcription factor dependencies. These data are particularly relevant given the recent development of clinical grade CDK7 inhibitors (Patel et al., 2018; Hu et al., 2019; S. Hu et al., 2019, Proc. Amer. Assoc. Cancer Res. Annu. Mtg, abstract). CDK7 inhibition with SY-5609 has already entered clinical trials (NCT04247126). Our focus on DNA repair is relevant to increasing radiation therapy sensitivity in high-risk patients. Targeting DNA repair disturbs transcriptionally active group 3 MB to enhance the impact of low-dosage RT and has potential to alleviate the neuronal deficiencies associated with treatment. Future developments of synergistic drug treatments with CDK7 inhibition are an alternative to delaying intensive treatments, obviating the need of RT in children younger than 3, providing more unimpeded time for essential neuronal development.

STAR★METHODS

RESOURCE AVAILABILITY

Lead contact—Further information and requests for resources and reagents should be directed to and will be fulfilled by the Lead Contact, Rajeev Vibhakar (Rajeev.vibhakar@cuanschutz.edu).

Materials availability—All unique/stable reagents and biological material generated in this study are available from the Lead Contact, Rajeev Vibhakar (Rajeev.vibhakar@cuanschutz.edu), with a completed Materials Transfer Agreement.

Date and code availability—The datasets generated during this study are available at GEO [GSE164933/ https://www.ncbi.nlm.nih.gov/geo/query/acc.cgi?acc=GSE164933] for RNA_seq and [GSE164696/ https://www.ncbi.nlm.nih.gov/geo/query/acc.cgi?acc=GSE164696] for ChIP-seq. Raw data from Figures 1, 2, 3, and S4A were deposited on Mendeley at http://data.mendeley.com/login?redirectPath=/datasets/x6nzmgx97h/draft?a=666c232d-8dd5-4046-8faa-f28109c48a4c. Additional datasets referenced in this study are available at [https://www.ncbi.nlm.nih.gov/geo/query/acc.cgi?acc=GSE62726].

EXPERIMENTAL MODELS AND SUBJECT DETAILS

Animal studies—Female athymic Nude-Foxn1^{nu} mice aged 4 to 8 weeks and female NOD-scid gamma aged 4 to 8 weeks were utilized for orthotopic xenograft studies. Mice were housed in ventilated cages with appropriate nesting enrichments, bedding, food and water according to the University of Colorado regulations. For D458/D425 genetic KD and D458/D425 treatment studies cells were collected and resuspended as a single cell suspension of 20000 cells/3 μL in serum free media. MED411 cells were injected at 200000/3 μL in serum free media. Intracranial injection of cells into outbred athymic Nude-Foxn1^{nu} mice (Jackson labs strain 07850) or NOD-scid gamma (Jackson labs strain 005557) was done at 1.5mm lateral and 2mm posterior of lambda at 400 nanoliters/min. Mice were monitored for tumor growth daily and euthanized when 15% weight loss was reached or signs of tumor (hunched back, paralysis, or tilted head) were evident. Littermates were randomly assigned to experimental groups. All animal procedures were performed in accordance with the National Research Council's Guide for the Care and Use of Laboratory Animals and were approved by the University of Colorado Anschutz Medical Campus Institutional Animal Care and Use Committee.

Cell lines—D425 (RRID:CVCL_1275; male) and D458 (RRID:CVCL_1161; male) cell lines were kindly provided by Dr. Darell D. Bigner (Duke University Medical Center, NC). Cells cultured in DMEM supplemented with 10% FBS (Sigma-Aldrich), 1 mM sodium pyruvate (GIBCO), 1 × penicillin/streptomycin solution (Cellgro), and with 1 × L-glutamine (Cellgro). DAOY (HTB-186; RRID:CVCL_1167; male) and D283 med (HTB-185; RRID:CVCL_1155; male) were obtained from ATCC and cultured in DMEM supplemented with 10% FBS (Sigma-Aldrich), 1 mM sodium pyruvate (GIBCO), 1mM NEAA(GIBCO), 1 × penicillin/streptomycin solution (Cellgro), and with 1 × L-glutamine (Cellgro). ONS76 (RRID:CVCL_1624; female) cells were obtained from Dr. James T. Rutka (The University of Toronto) and cultured in DMEM (GIBCO, Carlsbad, CA) supplemented with 10% FBS (Sigma-Aldrich) and 1 × penicillin/streptomycin solution (Cellgro). ONS76-RFP and ONS76-MYC cells were established as in Moreira et al. (2020), cells were exposed to 5ug/mL doxycycline to induce MYC expression 24 hours prior to experiment. RPE-Neo (RRID:CVCL_GQ00; female) and RPE-Myc cells were provided by Andre Goga (UCSF). UW228 (RRID:CVCL_4460; female) and NIH 3T3 (RRID:CVCL_0594;

male) were obtained from Dr John Silber at the University of Washington. NHA cells were provided by Cynthia Hawkins (University of Toronto Hospital for Sick Children). MED411FH was originally harvested from a large cell anaplastic medulloblastoma that was molecularly characterized as a group 3 tumor. All cell lines were cultured at 37°C with 95% air and 5% CO2. Cell lines were authenticated with STR fingerprinting using Globalfiler® System (Thermo Fisher Scientific) and processed on ABI 3500Xl Genetic Analyzer and mycoplasma testing was conducted with the Venor GeM Mycoplasma Detection Kit (Cat# MP0025–1kt, Sigma- Aldrich) both were done as recent as 1/9/2020. All cell lines were maintained for a maximum of 20 passages for the duration of experiments.

METHOD DETAILS

Viral transduction—CDK7 stable knockdown cell lines were established using gene specific mission shRNAs (Cat# TRCN0000000595, TRCN0000000592, TRCN0000230910) or non-targeting control (Sigma-Aldrich). HEK293FT cells were plated at 5×10^6 cells/10cm dish one day before transfection in complete media (DMEM, 10%FBS, 5% penicillin and streptomycin). Lipofectamine 3000 (Thermo Fisher Scientific, Cat#L3000008) was diluted in Opti-MEM at a ratio of 1:16.6. P3000 was diluted at 1:25 in Opti-MEM along with 1 μg pMD2.G, 2 μg psPAX2, and 1.2 μg pLenti-shCDK7 expression vector. Both mixes were combined and incubated for 15 mins at room temperature. The mixture was added dropwise to HEK293FT cells in fresh media. 24 hours later the media was replaced with DMEM/2.5% FBS. Viral particles were collected at 48 hours in a 15 mL conical and centrifuged for 5 min at 500xg. Virus was then filtered through a 0.45 micron filter and stored in 1 mL aliquots at −80. To generate the stable knockdown cell lines, cells were plated at 5×10^5 in a 6-well dish in growth medium containing 8μg/mL polybrene. Viral particles were added with 8μg/mL polybrene and incubated for 7 hr. Transduced cells were disaggregated, grown, and selected with 1μg/mL puromycin for 14 days. Transformants were confirmed by qRT-PCR and western blot.

Compounds—THZ1 (Cat #9002215) was purchased from Cayman Chemical. THZ2 (Cat #HY-12280/CS-3245) and CT7001 (Cat#HY-103712A) were purchased from MedChem Express. YKL-5–124 (Cat#S8863) was purchased from Selleckchem. Chemical compounds were diluted in DMSO at 10mM stock concentration. Working concentrations were then diluted in serum free media.

***In vivo* chemical treatment—**THZ2 was diluted in 5% dextrose w/v and delivered via intraperitoneal injection at 15mg/kg for 25 days, daily. Vehicle was 10% DMSO diluted in 5% dextrose w/v. A Kaplan-Meier plot was used for survival calculations. Brain tissue was collected following euthanasia and fixed in 10% formalin.

IC_{50} determination—Cells were plated at 1000 cells/well in a 96-well dish and exposed to DMSO, THZ1, or THZ2 for 48hrs at 0.005, 0.010, 0.05, 0.1, 0.25, 0.5, 1, 2, 5, 7, 10μM. Cell viability was assessed with CellTiter 96® Aqueous One Solution Cell Proliferation Assay #G3580 (Promega) as per manufactures' instructions.

Annexin V assay—Guava Nexin Assay #4500–0450 (Millipore). 2.0×10^5 cells were collected and stained in 100 μl of Guava Nexin reagent for 20min then collected on Guava system flow cytometer (Millipore).

CRISPR-Cas9 screen—The CU Druggable Library (CUDL) consists of 8 gRNA per gene and targets 1095 genes curated from the 667 human genes targeted by 1194 FDA-approved drugs (Santos et al., 2017) and 428 genes encoding known drug targets involved in metabolism, protein modifications, signal transduction, and macromolecular transport biased for receptors and kinases (Wang et al., 2014) and druggable genes of interest from multiple research labs in University of Colorado's Anschutz Medical Campus. The panel also consists of 500 non-targeting gRNA. The gRNAs were from https://personal.broadinstitute.org/timw/. CRISPR; Cas-OFFinder tool was used to determine the potential off-targets (Bae et al., 2014) and Rule Set 2 score to measure the on-target activity of each gRNA (Doench et al., 2016). The oligo pool for the gRNA library was synthesized on a chip (CustomArray), PCR amplified and cloned into lenti-CRISPRv2 (Addgene Plasmid #52961) and lentiGUIDE-puro (Addgene Plasmid #52963) (Sanjana et al., 2014) as described in Wang et al. (2016) and Joung et al. (2017). Next-generation sequencing of the amplified plasmid pool was performed to determine gRNA distribution.

Methylcellulose assays—500 cells/3 mL were plated in a 1:1 mixture of 2.6% methylcellulose and complete growth medium. Cells were allowed to grow for ten days. Colonies were stained with nitrotetrazolium blue chloride (Sigma) at 1.5mg/mL in PBS for 24hrs at 37°C then counted.

Neurosphere assay—D458 or D425 shNull and shCDK7 cells were serially diluted at 100,10, and single cell suspensions in neurosphere growth media (neurobasal medium, B-27+vitamin A, L-glutamine, pen/strep, EGF, and FGF). Cells were grown for fourteen days with media replacement every three days at 37°C. At fourteen days spheres were collected, disassociated, and replated at 100, 10, and single cell suspensions and allowed to grow for an additional fourteen days. Neurosphere proliferation and real time monitoring was done using the Incucyte® S3 live cell imaging system (Essen Bioscience).

RNA sequencing and analysis—Total RNA was isolated in triplicate from D458 cells treated with 10nM THZ1 or DMSO using RNeasy Mini kit (QIAGEN). RNA-seq was performed at Genomics and Microarray Core Facility, Anschutz Medical Campus using the illumina Novaseq 6000. High quality base calls at 95% ≥ Q30 were obtained with 53M-69M single reads. Statistical analysis of count data was performed with DESeq2 R package (Love et al., 2014). Further analysis by GSEA was performed using the MSigDB (Mootha et al., 2003; Subramanian et al., 2005) and DAVID functional classification tool was used for gene ontology comparison (Huang et al., 2009a, 2009b).

RNA isolation and cDNA synthesis—Total RNA was isolated from 1×10^6-1×10^7 cells with the RNeasy Mini kit (QIAGEN). 2 μg of isolated RNA was used to make cDNA using the High Capacity Reverse Transcription Kit (Thermo Fisher Scientific) as per manufacturer's instructions. cDNA was then diluted to 20ng/μL for qRT-PCR reactions.

qRT-PCR—TaqMan Universal Master Mix II, no UNG (Thermo Fisher Scientific) was used with gene specific TaqMan primers for all qRT-PCR reactions. 5 μL of the diluted cDNA was used per 20 μL PCR reaction. Reactions were conducted in triplicate and performed on a QuantStudio 5 Real Time PCR machine (Thermo Fisher Scientific). Analysis of cDNA transcripts was done using the comparative C_t method.

Western blot—Cells were lysed in RIPA buffer (Pierce, Thermo Fisher Scientific) containing an EDTA-free protease inhibitor (Roche), and protein concentrations were determined with the BCA Protein Assay Kit (Pierce, Thermo Fisher). 30μg of total protein was separated on a 4%–20% gradient SDS-PAGE (BioRad). Primary antibodies α-RNA Pol II CTD S2 #13499, α-RNA Pol II CTD S5 #13523, α-CDK7 #2916, α-CDK9 #2316, α-PARP #9542, α-cMYC #5605 (Cell Signaling Technology), and α-Total RNA Pol II #A300–653A (Bethyl Laboratories) were exposed overnight at 4°C. Secondary antibody, α-mouse-HRP Cat# 7076 and α-rabbit-HRP Cat# 7074 or α-Actin-HRP Cat# 12262 (Cell Signaling Technology), was exposed for 1hr at RT. Blots were developed with Luminata Forte Western HRP (Millipore) and imaged using Syngene GBox Chemi-SL1.4 gel doc. Western blots quantified using ImageJ (Schneider et al., 2012). Proteins were normalized to loading controls then compared to shNull or DMSO. Phospho-proteins were normalized to total protein/loading control.

Chromatin immunoprecipitation—Cells were collected at confluency or approximately 1 million cells/IP. Cells were washed with 1xPBS, cross-linked with 1% paraformaldehyde in PBS at RT, and quenched with 2.5M glycine. Cells were then washed with ice cold PBS and lysed in 1mL RIPA buffer (150mM NaCl, 1% v/v Nonidet P-40, 0.5% w/v deoxycholate, 0.1% w/v SDS, 50mM Tris pH 8.0, 5mM EDTA) plus inhibitors (leupeptin 1μg/mL, aprotinin 1μg/mL, pepstatin 1μg/mL, benzamidine 1mM, and PMSF 1mM). Lysates were sonicated using Diagenode Bioruptor® with 25 cycles of 30 s pulses and 90 s intervals to shear DNA to ~500 bp fragments. Lysates were then cleared by centrifugation at 12800 rpm for 15 min at 4°C. 40 μl of protein A/G Sepharose beads (Millipore) were added and the lysate was pre-cleared for 1 hr at 4°C. 20 μl of protein A/G beads blocked with 1mg/mL BSA was mixed with the pre-cleared lysate, and immunoprecipitation was carried out by adding 5–10 μg of antibody (α-RNA Pol II #ab817 abcam, α-cMYC #13987, cell signaling technology) rotating overnight at 4°C. Beads were washed 2x with RIPA, 4X with IP wash buffer (100mM TrisHCL pH8.5, 500mM LiCl, 1%v/v Nonidet-P-40, 1% w/v deoxycholic acid), and 2x with TE buffer. Immunocomplexes were eluted at 65°C with elution buffer (70mM TrisHCl pH 8, 1mM EDTA, 1.5% w/v SDS). The eluate was brought to a final concentration of 200mM NaCl and reverse crosslinked at 65°C. The eluate was then treated with proteinase K, and DNA was isolated by phenol/chloroform extraction and ethanol precipitation. ChIP-DNA was quantified using the Qubit® dsDNA High Sensitivity Assay kit (Thermo Fisher).

ChIP sequencing and analysis—Ovation UltraLow system V2 #0344 (Nugen) was used to prepare libraries as per protocol requirements. ChIP-seq libraries were sequenced on the Illumina Novaseq 6000 platform. 62M-69M reads with high quality base calls at 90% ≥ Q30 were obtained. Bowtie2 was used to align the 150-bp paired-end sequencing reads to a

reference human genome (hg19) downloaded from the UCSC Genome Browser. Unmapped and non-uniquely mapped reads were removed, and PCR duplicate reads were removed using samtools version 1.5. Peaks were called using MACS2 (v2.1.1.20160309) (Zhang et al., 2008) with default parameters. Peak locations were further annotated according to the known genes in hg38 and 3000 bp of upstream and downstream of transcription start sites were considered as promoter regions using the R/Bioconductor package ChIPseeker (Yu et al., 2015).

Bioluminescence imaging—IVIS imaging was conducted on the Xenogen IVIS200 Bioluminescence system (Perkin Elmer). Mice were injected intraperitoneally with Luciferin #LUCK-5g, CAS 115144-35-9 (GoldBio) at 10μl/g body weight. Mice were anesthetized at 2% isoflurane/oxygen mixture then photons/counts were measured at 30 s time intervals. Analysis of photon emissions was conducted using Living Image v2.60.1 software.

Magnetic resonance imaging (MRI)—For *in vivo* MRI acquisitions, mice were anesthetized shortly before and during the MRI session using 1.5% of isoflurane/ oxygen mixture. Anesthetized mice were placed on a temperature-controlled mouse bed below a mouse head array coil and inserted into Bruker 9.4 Tesla BioSpec MR scanner (Bruker Medical, Billerica, MA). First, T2-weighted turboRARE images were acquired using the following parameters: repetition time (TR) = 3268 ms, echo time (TE) = 60 ms, RARE factor = 12, 8 averages, FOV = 20 mm, matrix size = 350 × 350, slice thickness = 700 μm, 24 sagittal and axial slices, in-plane spatial resolution = 51 μm. Then, diffusion weighted EPI sequence with 6 b-values was used using 4 axial slices covering the entire tumor lesions\ and unaffected brain tissue. Tumor regions were manually segmented on T2-weighted images by placing hand-drawing regions of interest (ROI) and the volume calculated as mm^3. The apparent diffusion coefficients (ADC, s/mm^2) were calculated from DWI maps as a criterion for tumor cellularity. All acquisitions and image analysis were performed using Bruker ParaVision NEO software.

Irradiation of culture cells and animals—Cultured cells were irradiated with a cesium-137 source (JL Shepherd Model 81–14R research irradiator) in 2 gray intervals from 0–10 gray.

Animal radiotherapy was performed using the X-Rad SmART small animal irradiator (Precision X-Ray, North Branford CT). Under isoflurane anesthesia, mice received 7.5Gy to the cerebellum, in 5 fractions of 1.5Gy, delivered on consecutive days with pairs of 10mm-diameter lateral beams.

Histological and immunofluorescence staining and microscopy—Fixed tissue was submitted to the University of Colorado Denver Tissue Histology Shared Resource for paraffin embedding, sectioning, and staining. Tissue was stained with α-CDK7 #2916, α-cleaved caspase 3 #9661, α-γH2AX #9718, α-RPA70/RPA1 #2267 (Cell Signaling Technology), α-Ki67#RM-9106 (Thermo Fisher) and α-RAD51 #NB100–148 (Novus Biological). Images were captured on Keyence BZ-X700 series microscope with the same exposure parameters at 4X and 20X then quantified with ImageJ.

QUANTIFICATION AND STATISTICAL ANALYSIS

All experiments were performed with at least three independent replications. All data was collected in Excel, and Graphpad Prism 9 statistical software was used for analysis. The mean ± SD is graphed. P values < 0.05 were considered significant, where p value < 0.05 (*), p value < 0.01(**), p value < 0.001 (***), p value < 0.0001 (****). Unpaired, two-tailed, t tests were used for two-group comparisons, and ANOVA analysis and Dunnett's test for multiple group comparisons.

Supplementary Material

Refer to Web version on PubMed Central for supplementary material.

ACKNOWLEDGMENTS

We would like to thank Dr. Darell D. Bigner (Duke University) for generously providing the D458 cell line used in this study. The authors appreciate the contribution made by the University of Colorado Denver Tissue Histology Shared Resource, supported in part by the Cancer Center Support Grant (P30CA046934). We thank the University of Colorado Cancer Center Functional Genomics core facility for lentiviral constructs and the Genomics and Microarray Shared Resource for their assistance with RNA sequencing and ChIP sequencing. The authors thank Jenna Steiner from the Colorado Animal Imaging Shared Resource (AISR) for acquiring all mouse MRI scans and Benjamin Van Court for animal radiography. The AISR is supported by the University of Colorado Cancer Center, the P30CA046934 Cancer Center, and S10 OD023485 High-End Shared Instrumentation grants (N.J.S.). This work was supported by the Morgan Adams Foundation (R.V. and S.V.), Cancer League of Colorado (R.V.), The Adam Crocker Fund for Cancer research (RV) and NIH grant R01NS088283.

REFERENCES

Adhikary S, and Eilers M (2005). Transcriptional regulation and transformation by Myc proteins. Nat. Rev. Mol. Cell Biol 6, 635–645. [PubMed: 16064138]

Alimova I, Venkataraman S, Harris P, Marquez VE, Northcott PA, Dubuc A, Taylor MD, Foreman NK, and Vibhakar R (2012). Targeting the enhancer of zeste homologue 2 in medulloblastoma. Int. J. Cancer 131, 1800–1809. [PubMed: 22287205]

Alimova I, Birks DK, Harris PS, Knipstein JA, Venkataraman S, Marquez VE, Foreman NK, and Vibhakar R (2013). Inhibition of EZH2 suppresses self-renewal and induces radiation sensitivity in atypical rhabdoid teratoid tumor cells. Neuro-oncol. 15, 149–160. [PubMed: 23190500]

Bae S, Park J, and Kim JS (2014). Cas-OFFinder: a fast and versatile algorithm that searches for potential off-target sites of Cas9 RNA-guided endonucleases. Bioinformatics 30, 1473–1475. [PubMed: 24463181]

Baluapuri A, Hofstetter J, Dudvarski Stankovic N, Endres T, Bhandare P, Vos SM, Adhikari B, Schwarz JD, Narain A, Vogt M, et al. (2019). MYC Recruits SPT5 to RNA Polymerase II to Promote Processive Transcription Elongation. Mol. Cell 74, 674–687.e11. [PubMed: 30928206]

Bradner JE, Hnisz D, and Young RA (2017). Transcriptional Addiction in Cancer. Cell 168, 629–643. [PubMed: 28187285]

Campaner S, and Amati B (2012). Two sides of the Myc-induced DNA damage response: from tumor suppression to tumor maintenance. Cell Div. 7, 6. [PubMed: 22373487]

Cavalli FMG, Remke M, Rampasek L, Peacock J, Shih DJH, Luu B, Garzia L, Torchia J, Nor C, Morrissy AS, et al. (2017a). Intertumoral Heterogeneity within Medulloblastoma Subgroups. Cancer Cell 31, 737–754.e6. [PubMed: 28609654]

Cavalli FMG, Remke M, Rampasek L, Peacock J, Shih DJH, Luu B, Garzia L, Torchia J, Nor C, Morrissy AS, et al. (2017b). Intertumoral Heterogeneity within Medulloblastoma Subgroups. Cancer Cell 31, 737–754.e6. [PubMed: 28609654]

Chen FX, Smith ER, and Shilatifard A (2018). Born to run: control of transcription elongation by RNA polymerase II. Nat. Rev. Mol. Cell Biol 19, 464–478. [PubMed: 29740129]

Chipumuro E, Marco E, Christensen CL, Kwiatkowski N, Zhang T, Hatheway CM, Abraham BJ, Sharma B, Yeung C, Altabef A, et al. (2014). CDK7 inhibition suppresses super-enhancer-linked oncogenic transcription in MYCN-driven cancer. Cell 159, 1126–1139. [PubMed: 25416950]

Christensen CL, Kwiatkowski N, Abraham BJ, Carretero J, Al-Shahrour F, Zhang T, Chipumuro E, Herter-Sprie GS, Akbay EA, Altabef A, et al. (2014). Targeting transcriptional addictions in small cell lung cancer with a covalent CDK7 inhibitor. Cancer Cell 26, 909–922. [PubMed: 25490451]

Cook Sangar ML, Genovesi LA, Nakamoto MW, Davis MJ, Knobluagh SE, Ji P, Millar A, Wainwright BJ, and Olson JM (2017). Inhibition of CDK4/6 by Palbociclib Significantly Extends Survival in Medulloblastoma Patient-Derived Xenograft Mouse Models. Clin. Cancer Res 23, 5802–5813. [PubMed: 28637687]

Core L, and Adelman K (2019). Promoter-proximal pausing of RNA polymerase II: a nexus of gene regulation. Genes Dev. 33, 960–982. [PubMed: 31123063]

Dhall G (2009). Medulloblastoma. J. Child Neurol 24, 1418–1430. [PubMed: 19841429]

Doench JG, Fusi N, Sullender M, Hegde M, Vaimberg EW, Donovan KF, Smith I, Tothova Z, Wilen C, Orchard R, et al. (2016). Optimized sgRNA design to maximize activity and minimize off-target effects of CRISPR-Cas9. Nat. Biotechnol 34, 184–191. [PubMed: 26780180]

Dubbury SJ, Boutz PL, and Sharp PA (2018). CDK12 regulates DNA repair genes by suppressing intronic polyadenylation. Nature 564, 141–145. [PubMed: 30487607]

El-Sheikh A, Fan R, Birks D, Donson A, Foreman NK, and Vibhakar R (2010). Inhibition of Aurora Kinase A enhances chemosensitivity of medulloblastoma cell lines. Pediatr. Blood Cancer 55, 35–41. [PubMed: 20232424]

Fisher RP (2018). Cdk7: a kinase at the core of transcription and in the cross-hairs of cancer drug discovery. Transcription 10, 47–56. [PubMed: 30488763]

Glover-Cutter K, Larochelle S, Erickson B, Zhang C, Shokat K, Fisher RP, and Bentley DL (2009). TFIIH-associated Cdk7 kinase functions in phosphorylation of C-terminal domain Ser7 residues, promoter-proximal pausing, and termination by RNA polymerase II. Mol. Cell. Biol 29, 5455–5464. [PubMed: 19667075]

Harris PS, Venkataraman S, Alimova I, Birks DK, Donson AM, Knipstein J, Dubuc A, Taylor MD, Handler MH, Foreman NK, and Vibhakar R (2012). Polo-like kinase 1 (PLK1) inhibition suppresses cell growth and enhances radiation sensitivity in medulloblastoma cells. BMC Cancer 12, 80. [PubMed: 22390279]

Harris PS, Venkataraman S, Alimova I, Birks DK, Balakrishnan I, Cristiano B, Donson AM, Dubuc AM, Taylor MD, Foreman NK, et al. (2014). Integrated genomic analysis identifies the mitotic checkpoint kinase WEE1 as a novel therapeutic target in medulloblastoma. Mol. Cancer 13, 72. [PubMed: 24661910]

Higdon R, Kala J, Wilkins D, Yan JF, Sethi MK, Lin L, Liu S, Montague E, Janko I, Choiniere J, et al. (2017). Integrated Proteomic and Transcriptomic-Based Approaches to Identifying Signature Biomarkers and Pathways for Elucidation of Daoy and UW228 Subtypes. Proteomes 5, 5. [PubMed: 28248256]

Hu S, Marineau JJ, Rajagopal N, Hamman KB, Choi YJ, Schmidt DR, Ke N, Johannessen L, Bradley MJ, Orlando DA, et al. (2019). Discovery and Characterization of SY-1365, a Selective, Covalent Inhibitor of CDK7. Cancer Res. 79, 3479–3491. [PubMed: 31064851]

Huang W, Sherman BT, and Lempicki RA (2009a). Bioinformatics enrichment tools: paths toward the comprehensive functional analysis of large gene lists. Nucleic Acids Res. 37, 1–13. [PubMed: 19033363]

Huang W, Sherman BT, and Lempicki RA (2009b). Systematic and integrative analysis of large gene lists using DAVID bioinformatics resources. Nat. Protoc 4, 44–57. [PubMed: 19131956]

Ira G, Pellicioli A, Balijja A, Wang X, Fiorani S, Carotenuto W, Liberi G, Bressan D, Wan L, Hollingsworth NM, et al. (2004). DNA end resection, homologous recombination and DNA damage checkpoint activation require CDK1. Nature 431, 1011–1017. [PubMed: 15496928]

Joung J, Konermann S, Gootenberg JS, Abudayyeh OO, Platt RJ, Brigham MD, Sanjana NE, and Zhang F (2017). Genome-scale CRISPR-Cas9 knockout and transcriptional activation screening. Nat. Protoc 12, 828–863. [PubMed: 28333914]

Kanin EI, Kipp RT, Kung C, Slattery M, Viale A, Hahn S, Shokat KM, and Ansari AZ (2007). Chemical inhibition of the TFIIH-associated kinase Cdk7/Kin28 does not impair global mRNA synthesis. Proc. Natl. Acad. Sci. USA 104, 5812–5817. [PubMed: 17392431]

Kann BH, Park HS, Lester-Coll NH, Yeboa DN, Benitez V, Khan AJ, Bindra RS, Marks AM, and Roberts KB (2016). Postoperative Radiotherapy Patterns of Care and Survival Implications for Medulloblastoma in Young Children. JAMA Oncol. 2, 1574–1581. [PubMed: 27491009]

Kool M, Korshunov A, Remke M, Jones DT, Schlanstein M, Northcott PA, Cho YJ, Koster J, Schouten-van Meeteren A, van Vuurden D, et al. (2012). Molecular subgroups of medulloblastoma: an international meta-analysis of transcriptome, genetic aberrations, and clinical data of WNT, SHH, Group 3, and Group 4 medulloblastomas. Acta Neuropathol. 123, 473–484. [PubMed: 22358457]

Krajewska M, Dries R, Grassetti AV, Dust S, Gao Y, Huang H, Sharma B, Day DS, Kwiatkowski N, Pomaville M, et al. (2019). CDK12 loss in cancer cells affects DNA damage response genes through premature cleavage and polyadenylation. Nat. Commun 10, 1757. [PubMed: 30988284]

Kress TR, Sabò A, and Amati B (2015). MYC: connecting selective transcriptional control to global RNA production. Nat. Rev. Cancer 15, 593–607. [PubMed: 26383138]

Kwiatkowski N, Zhang T, Rahl PB, Abraham BJ, Reddy J, Ficarro SB, Dastur A, Amzallag A, Ramaswamy S, Tesar B, et al. (2014). Targeting transcription regulation in cancer with a covalent CDK7 inhibitor. Nature 511, 616–620. [PubMed: 25043025]

Langmead B, Trapnell C, Pop M, and Salzberg SL (2009). Ultrafast and memory-efficient alignment of short DNA sequences to the human genome. Genome Biol. 10, R25. [PubMed: 19261174]

Larochelle S, Merrick KA, Terret ME, Wohlbold L, Barboza NM, Zhang C, Shokat KM, Jallepalli PV, and Fisher RP (2007). Requirements for Cdk7 in the assembly of Cdk1/cyclin B and activation of Cdk2 revealed by chemical genetics in human cells. Mol. Cell 25, 839–850. [PubMed: 17386261]

Larochelle S, Amat R, Glover-Cutter K, Sansó M, Zhang C, Allen JJ, Shokat KM, Bentley DL, and Fisher RP (2012). Cyclin-dependent kinase control of the initiation-to-elongation switch of RNA polymerase II. Nat. Struct. Mol. Biol 19, 1108–1115. [PubMed: 23064645]

Li H, Handsaker B, Wysoker A, Fennell T, Ruan J, Homer N, Marth G, Abecasis G, and Durbin R; 1000 Genome Project Data Processing Subgroup (2009). The Sequence Alignment/Map format and SAMtools. Bioinformatics 25, 2078–2079. [PubMed: 19505943]

Liu F, Jiang W, Sui Y, Meng W, Hou L, Li T, Li M, Zhang L, Mo J, Wang J, et al. (2019). CDK7 inhibition suppresses aberrant hedgehog pathway and overcomes resistance to smoothened antagonists. Proc. Natl. Acad. Sci. USA 116, 12986–12995. [PubMed: 31182587]

Love MI, Huber W, and Anders S (2014). Moderated estimation of fold change and dispersion for RNA-seq data with DESeq2. Genome Biol. 15, 550. [PubMed: 25516281]

Lu P, Geng J, Zhang L, Wang Y, Niu N, Fang Y, Liu F, Shi J, Zhang ZG, Sun YW, et al. (2019). THZ1 reveals CDK7-dependent transcriptional addictions in pancreatic cancer. Oncogene 38, 3932–3945. [PubMed: 30692639]

Mootha VK, Lindgren CM, Eriksson KF, Subramanian A, Sihag S, Lehar J, Puigserver P, Carlsson E, Ridderstråle M, Laurila E, et al. (2003). PGC-1alpha-responsive genes involved in oxidative phosphorylation are coordinately downregulated in human diabetes. Nat. Genet 34, 267–273. [PubMed: 12808457]

Moreira DC, Venkataraman S, Subramanian A, Desisto J, Balakrishnan I, Prince E, Pierce A, Griesinger A, Green A, Eberhardt CG, et al. (2020). Targeting MYC-driven replication stress in medulloblastoma with AZD1775 and gemcitabine. J. Neurooncol 147, 531–545. [PubMed: 32180106]

Nagaraja S, Vitanza NA, Woo PJ, Taylor KR, Liu F, Zhang L, Li M, Meng W, Ponnuswami A, Sun W, et al. (2017). Transcriptional Dependencies in Diffuse Intrinsic Pontine Glioma. Cancer Cell 31, 635–652.e6. [PubMed: 28434841]

Northcott PA, Korshunov A, Pfister SM, and Taylor MD (2012a). The clinical implications of medulloblastoma subgroups. Nat. Rev. Neurol 8, 340–351. [PubMed: 22565209]

Northcott PA, Shih DJ, Peacock J, Garzia L, Morrissy AS, Zichner T, Stutz AM, Korshunov A, Reimand J, Schumacher SE, et al. (2012b). Subgroup-specific structural variation across 1,000 medulloblastoma genomes. Nature 488, 49–56. [PubMed: 22832581]

Northcott PA, Robinson GW, Kratz CP, Mabbott DJ, Pomeroy SL, Clifford SC, Rutkowski S, Ellison DW, Malkin D, Taylor MD, et al. (2019). Medulloblastoma. Nat. Rev. Dis. Primers 5, 11. [PubMed: 30765705]

Olson CM, Liang Y, Leggett A, Park WD, Li L, Mills CE, Elsarrag SZ, Ficarro SB, Zhang T, Düster R, et al. (2019). Development of a Selective CDK7 Covalent Inhibitor Reveals Predominant Cell-Cycle Phenotype. Cell Chem. Biol 26, 792–803.e10. [PubMed: 30905681]

Patel H, Periyasamy M, Sava GP, Bondke A, Slafer BW, Kroll SHB, Barbazanges M, Starkey R, Ottaviani S, Harrod A, et al. (2018). ICEC0942, an Orally Bioavailable Selective Inhibitor of CDK7 for Cancer Treatment. Mol. Cancer Ther 17, 1156–1166. [PubMed: 29545334]

Ramaswamy V, Remke M, Bouffet E, Bailey S, Clifford SC, Doz F, Kool M, Dufour C, Vassal G, Milde T, et al. (2016). Risk stratification of childhood medulloblastoma in the molecular era: the current consensus. Acta Neuropathol. 131, 821–831. [PubMed: 27040285]

Rimel JK, Poss ZC, Erickson B, Maas ZL, Ebmeier CC, Johnson JL, Decker TM, Yaron TM, Bradley MJ, Hamman KB, et al. (2020). Selective inhibition of CDK7 reveals high-confidence targets and new models for TFIIH function in transcription. Genes Dev. 34, 1452–1473. [PubMed: 33060135]

Ryan SL, Schwalbe EC, Cole M, Lu Y, Lusher ME, Megahed H, O'Toole K, Nicholson SL, Bognar L, Garami M, et al. (2012). MYC family amplification and clinical risk-factors interact to predict an extremely poor prognosis in childhood medulloblastoma. Acta Neuropathol. 123, 501–513. [PubMed: 22139329]

Sanjana NE, Shalem O, and Zhang F (2014). Improved vectors and genome-wide libraries for CRISPR screening. Nat. Methods 11, 783–784. [PubMed: 25075903]

Santos R, Ursu O, Gaulton A, Bento AP, Donadi RS, Bologa CG, Karlsson A, Al-Lazikani B, Hersey A, Oprea TI, and Overington JP (2017). A comprehensive map of molecular drug targets. Nat. Rev. Drug Discov 16, 19–34. [PubMed: 27910877]

Schneider CA, Rasband WS, and Eliceiri KW (2012). NIH Image to ImageJ: 25 years of image analysis. Nat. Methods 9, 671–675. [PubMed: 22930834]

Schwalbe EC, Lindsey JC, Nakjang S, Crosier S, Smith AJ, Hicks D, Rafiee G, Hill RM, Iliasova A, Stone T, et al. (2017). Novel molecular subgroups for clinical classification and outcome prediction in childhood medulloblastoma: a cohort study. Lancet Oncol. 18, 958–971. [PubMed: 28545823]

Serizawa H, Conaway JW, and Conaway RC (1993). Phosphorylation of C-terminal domain of RNA polymerase II is not required in basal transcription. Nature 363, 371–374. [PubMed: 8497323]

Singh SK, Clarke ID, Terasaki M, Bonn VE, Hawkins C, Squire J, and Dirks PB (2003). Identification of a cancer stem cell in human brain tumors. Cancer Res. 63, 5821–5828. [PubMed: 14522905]

Subramanian A, Tamayo P, Mootha VK, Mukherjee S, Ebert BL, Gillette MA, Paulovich A, Pomeroy SL, Golub TR, Lander ES, and Mesirov JP (2005). Gene set enrichment analysis: a knowledge-based approach for interpreting genome-wide expression profiles. Proc. Natl. Acad. Sci. USA 102, 15545–15550. [PubMed: 16199517]

Swartling FJ, Grimmer MR, Hackett CS, Northcott PA, Fan QW, Goldenberg DD, Lau J, Masic S, Nguyen K, Yakovenko S, et al. (2010). Pleiotropic role for MYCN in medulloblastoma. Genes Dev. 24, 1059–1072. [PubMed: 20478998]

Taylor MD, Northcott PA, Korshunov A, Remke M, Cho YJ, Clifford SC, Eberhart CG, Parsons DW, Rutkowski S, Gajjar A, et al. (2012). Molecular subgroups of medulloblastoma: the current consensus. Acta Neuropathol. 123, 465–472. [PubMed: 22134537]

Thorvaldsdóttir H, Robinson JT, and Mesirov JP (2013). Integrative Genomics Viewer (IGV): high-performance genomics data visualization and exploration. Brief. Bioinform 14, 178–192. [PubMed: 22517427]

van Riggelen J, Yetil A, and Felsher DW (2010). MYC as a regulator of ribosome biogenesis and protein synthesis. Nat. Rev. Cancer 10, 301–309. [PubMed: 20332779]

Venkataraman S, Alimova I, Balakrishnan I, Harris P, Birks DK, Griesinger A, Amani V, Cristiano B, Remke M, Taylor MD, et al. (2014). Inhibition of BRD4 attenuates tumor cell self-renewal and suppresses stem cell signaling in MYC driven medulloblastoma. Oncotarget 5, 2355–2371. [PubMed: 24796395]

Veo B, Danis E, Pierce A, Sola I, Wang D, Foreman NK, Jin J, Ma A, Serkova N, Venkataraman S, and Vibhakar R (2019). Combined functional genomic and chemical screens identify SETD8 as a therapeutic target in MYC-driven medulloblastoma. JCI Insight 4, e122933. [PubMed: 30626740]

Wang P, Lin SL, Zhang LH, Li Z, Liu Q, Gao JX, Liu DM, Bo JJ, and Huang YR (2014). The prognostic value of P-cadherin in non-muscle-invasive bladder cancer. Eur. J. Surg. Oncol 40, 255–259. [PubMed: 24429027]

Wang T, Lander ES, and Sabatini DM (2016). Single Guide RNA Library Design and Construction. Cold Spring Harb. Protoc 2016, pdb.prot090803.

Wang Y, Zhang T, Kwiatkowski N, Abraham BJ, Lee TI, Xie S, Yuzugullu H, Von T, Li H, Lin Z, et al. (2015). CDK7-dependent transcriptional addiction in triple-negative breast cancer. Cell 163, 174–186. [PubMed: 26406377]

Whiteway SL, Harris PS, Venkataraman S, Alimova I, Birks DK, Donson AM, Foreman NK, and Vibhakar R (2013). Inhibition of cyclin-dependent kinase 6 suppresses cell proliferation and enhances radiation sensitivity in medulloblastoma cells. J. Neurooncol 111, 113–121. [PubMed: 23138228]

Yu G, Wang LG, and He QY (2015). ChIPseeker: an R/Bioconductor package for ChIP peak annotation, comparison and visualization. Bioinformatics 31, 2382–2383. [PubMed: 25765347]

Zhang H, Christensen CL, Dries R, Oser MG, Deng J, Diskin B, Li F, Pan Y, Zhang X, Yin Y, et al. (2020). CDK7 Inhibition Potentiates Genome Instability Triggering Anti-tumor Immunity in Small Cell Lung Cancer. Cancer Cell 37, 37–54.e9. [PubMed: 31883968]

Zhang Y, Liu T, Meyer CA, Eeckhoute J, Johnson DS, Bernstein BE, Nusbaum C, Myers RM, Brown M, Li W, and Liu XS (2008). Model-based analysis of ChIP-Seq (MACS). Genome Biol. 9, R137. [PubMed: 18798982]

Zhou Y, Zhou B, Pache L, Chang M, Khodabakhshi AH, Tanaseichuk O, Benner C, and Chanda SK (2019). Metascape provides a biologist-oriented resource for the analysis of systems-level datasets. Nat. Commun 10, 1523. [PubMed: 30944313]

Highlights

- CDK7 is an essential factor mediating MYC-amplified medulloblastoma growth
- CDK7 inhibition reduces RNA Pol II and MYC at the TSS of a core set of genes
- Chemical inhibition of CDK7 exposes vulnerabilities in DNA repair gene networks
- Inhibiting CDK7 enhances radiation sensitivity in medulloblastoma xenografts

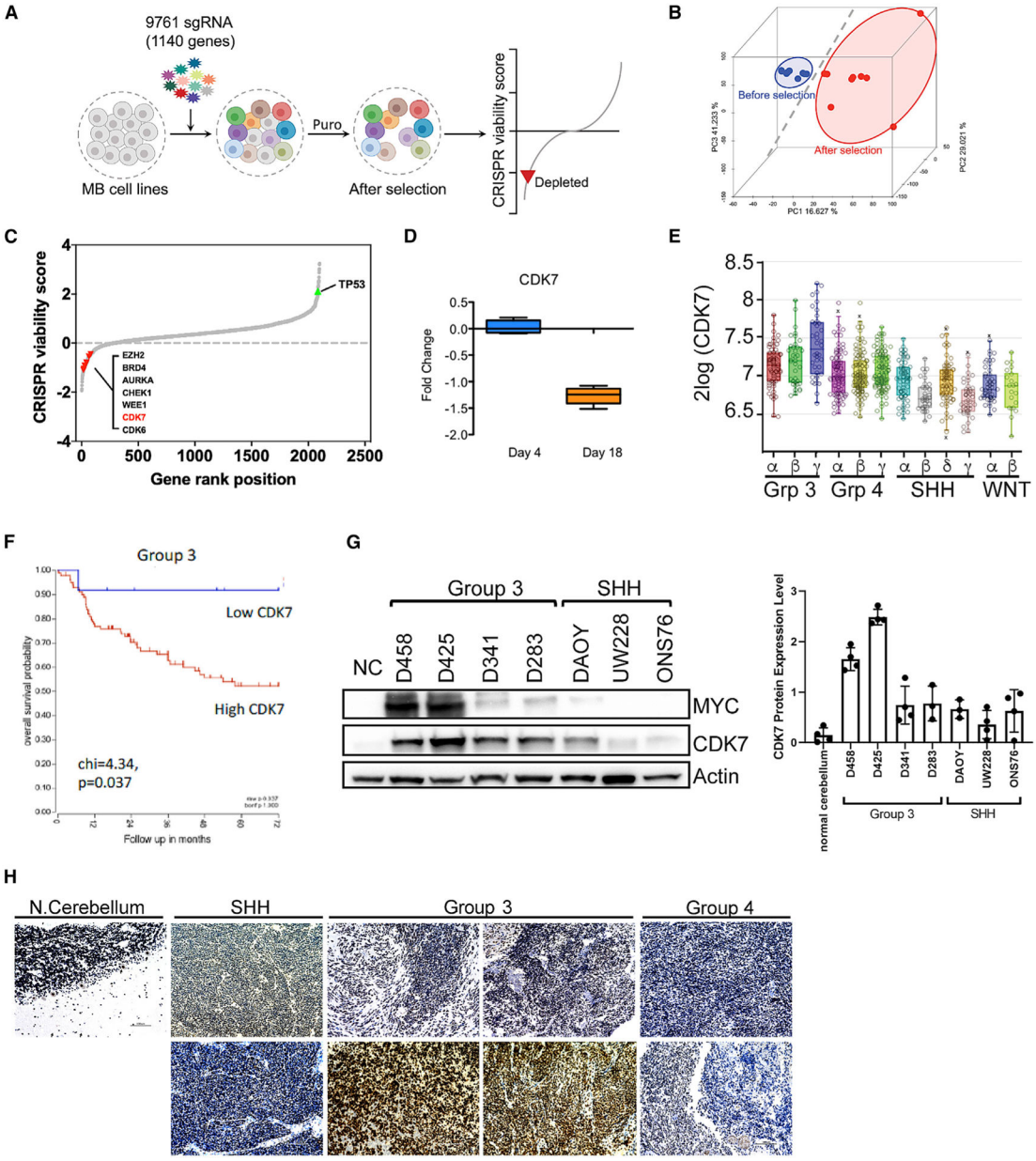

Figure 1. CDK7 expression in MB enhanced in group 3 tumors

(A) Graphic of the Crispr-Cas9 druggable kinase screen performed on three group 3 MB cell lines.

(B) Principal-component analysis (PCA) plot of before and after puromycin selection.

(C) S curve plot. Previously identified genes are in black, and new genes are in red.

(D) The fold change expression of CDK7 sgRNA.

(E) CDK7 expression in MB by subtype.

(F) Patient overall survival in group 3 MB in relation to CDK7 expression. n = 113.

(G) Immunoblot of CDK7 protein in four group 3 MB and three SHH MB cell lines. n = 4. Quantification of CDK7 expression is normalized to actin (right). Mean ± SD.

(H) IHC of CDK7 in normal cerebellum. Black arrows indicate positive brown cells, two SHH, four group 3, and two group 4 patient tumors. Scale bar, 100 μm.
See also Figure S1.

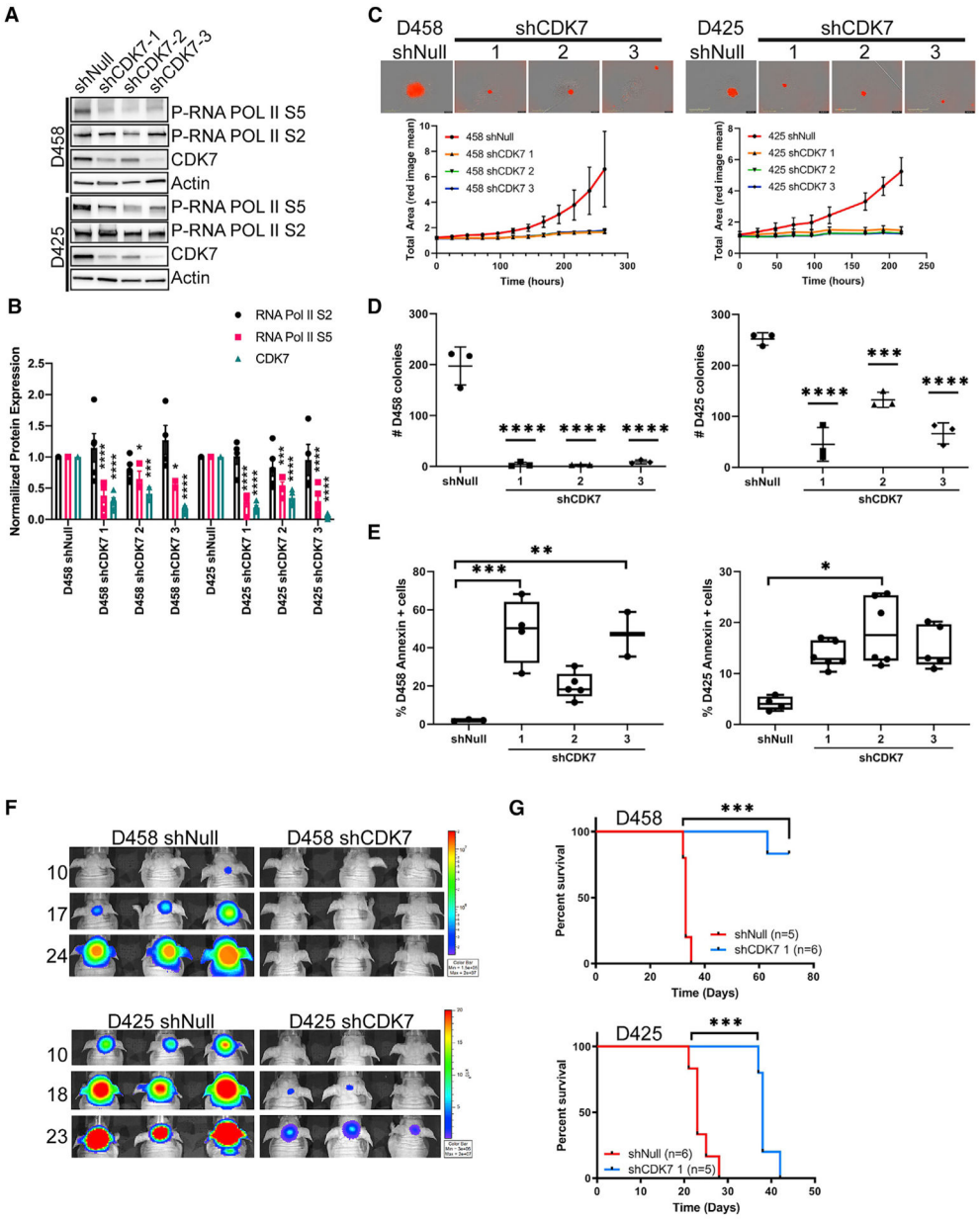

Figure 2. Genetic depletion of CDK7 decreases proliferation and tumor growth

(A) Immunoblot for indicated proteins of lysates transduced with three shRNAs against CDK7 or shNull.

(B) Quantification of (A). n = 3, mean ± SD. Statistical analysis, two-way ANOVA, ****p < 0.0001; ***p < 0.001; *p < 0.05.

(C) Neurosphere assay growth in CDK7-depleted D458 or D425 MB cell lines. Representative images at 10 days are shown. Total average growth of neurospheres was determined by NucRed fluorescence. n = 3, mean ± SD. Scale bar, 400 μm.

(D) Methylcellulose assay colony count of CDK7 KD cell lines (D458,D425). n = 3. Scatterplot, mean ± SD. Statistical analysis, two-way ANOVA. ****p < 0.0001; ***p < 0.001.

(E) Annexin V (+) staining assay. D458 and D425 KD cells were stained for Annexin V and measured by guava flow cytometry. Box and whisker ± min and max plot of the percentage of Annexin V (+) stained cells (y axis). n = 3. Statistical analysis, two-way ANOVA. ***$p < 0.001$; **$p < 0.005$; *$p < 0.05$.

(F) Representative bioluminescence images of xenograft D458 shCDK7 and D425 shCDK7 or shNull. Shown are days post-injection (left). Color scales indicate bioluminescence radiance in photons/sec/cm^2/steradian (right).

(G) Kaplan-Meier survival curve of D458 CDK7 KD (n = 6) and shNull (n = 5), (top). Also shown are D425 shNull (n = 6) or shCDK7 (n = 5) (bottom). Statistical analysis log-rank (Mantel-Cox) test; ***$p < 0.001$.

See also Figure S2.

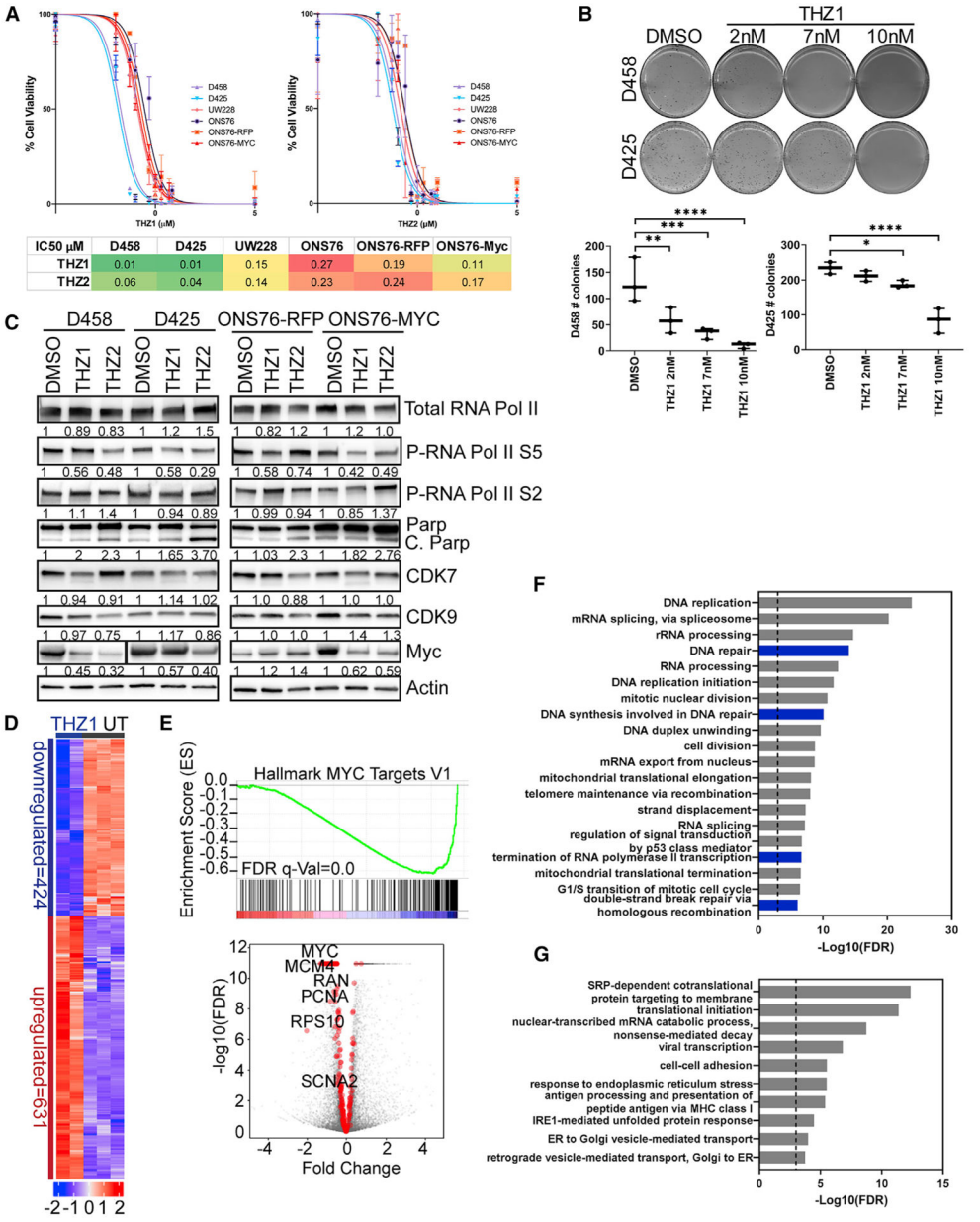

Figure 3. Low-dose THZ1 silences MYC-activated genes

(A) Log IC_{50} determination of THZ1 and THZ2 on group 3 MB cell lines and non-MYC-amplified cell lines. n = 3. Mean ± SEM. Color scale indicates low (green) to high (red) concentrations.

(B) Representative images of methylcellulose assay of D458 or D425 cells treated with DMSO or 2 (IC20), 7 (IC30), or 10 nM (IC_{50}) THZ1. n = 3. Scatterplot of colonies/well, mean ± SD. Statistical analysis, one-way ANOVA. ****p < 0.0001; ***p < 0.001; **p < 0.01; *p < 0.05.

(C) Immunoblot of proteins from D458, D425, ONS76-RFP, and ONS76-MYC treated with IC_{50} of THZ1 or THZ2 Average density below blot, n = 3. See also Figures S3D and S3E for quantification (CPARP, cleaved PARP).

(D) RNA-seq gene expression heatmap of THZ1 IC_{50} treated D458 and untreated cells. Calculated *Z* score scale is shown.
(E) GSEA Hallmark MYC targets V1 of genes downregulated by THZ1 treatment. False discovery rate (FDR) q value = 0.0. (top). Volcano plot of gene expression changes in hallmark MYC targets V2, shown in red. All genes are in gray (bottom).
(F) GO terms for THZ1-treated D458 of downregulated gene set from RNA-seq data. Shown are −log10(FDR) values, where the dotted line indicates FDR < 0.001. DNA-repair-related categories are shown in blue.
(G) GO terms for THZ1-treated D458 of upregulated gene set from RNA-seq data. Shown are −log10(FDR) values, where the dotted line indicates FDR < 0.001.
See also Figure S3.

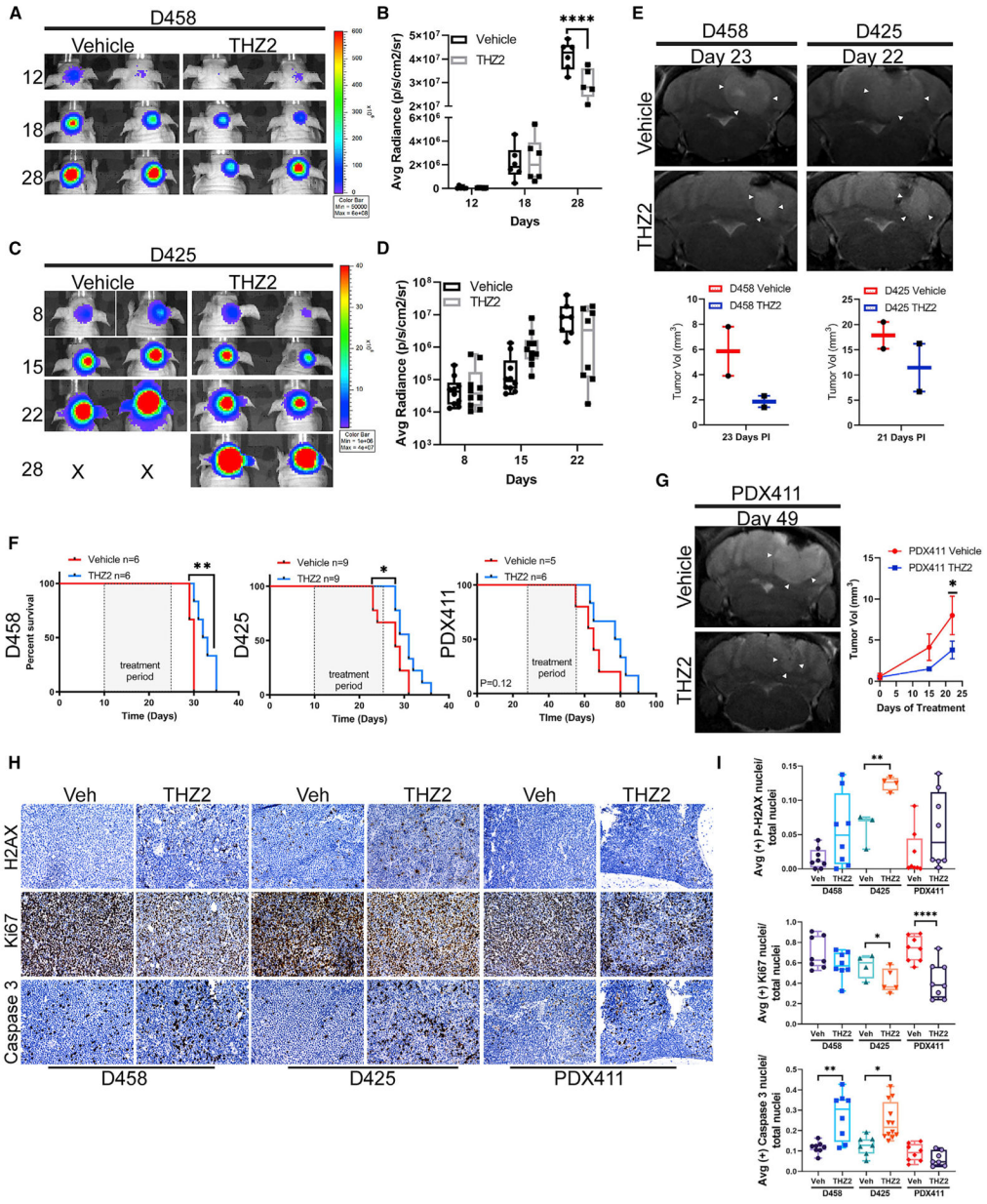

Figure 4. *In vivo* efficacy of CDK7 inhibition

(A) Nude mice xenografts injected with D458 cells were treated with vehicle (n = 6) or THZ2 (n = 6) 15 mg/kg daily. Representative images of bioluminescence imaging at 12, 18, and 28 days post-injection are shown. Color scales indicate bioluminescence radiance in photons/sec/cm^2/steradian.

(B) Box-and-whisker plot ± min and max of mean total radiance in photons/sec/cm^2/steradian (plotted from A). Statistical analysis, two-way ANOVA. ****$p < 0.0001$.

(C) D425 nude mice xenografts treated with vehicle (n = 9) and THZ2 (n = 9) 15 mg/kg daily. Representative images show bioluminescence imaging at days 8, 15, and 22. Color scales indicate bioluminescence radiance in photons/sec/cm^2/steradian. X, mouse death.

(D) Box-and-whisker plot ± min and max of mean total radiance in photons/sec/cm^2/steradian (plotted from C).
(E) Representative MRI of two vehicle- and THZ2-treated D458 and D425 xenografts (top). White arrows indicate tumor edge. Tumor volume in mm^3 (y axis) in vehicle- and THZ2-treated mice for D458 and D425 (bottom).
(F) Kaplan-Meier survival curve of D458, D425, and PDX411 xenograft mice treated with vehicle or THZ2. Treatment period for 25 days is shown in the shaded box. Statistical analysis log-rank (Mantel-Cox) test, **$p < 0.005$; *$p < 0.05$.
(G) PDX411 MRI and tumor volume in mm^3 (y axis) at 28, 42, and 49 days post-injection. Mean ± SEM. Statistical analysis, two-way ANOVA, *$p < 0.05$.
(H) Representative IHC staining for P-H2AX, Ki67, and caspase-3 of D458, D425, and PDX411 tumors from vehicle- and THZ2-treated mice. Scale bar, 100 μm.
(I) Box-and-whisker plots ± min and max of IHC quantifications. Representative images (n = 4) from two tumors from each cohort. Statistical analysis, one-way ANOVA. ****$p < 0.0001$; **$p < 0.01$; *$p < 0.05$.
See also Figures S3 and S4.

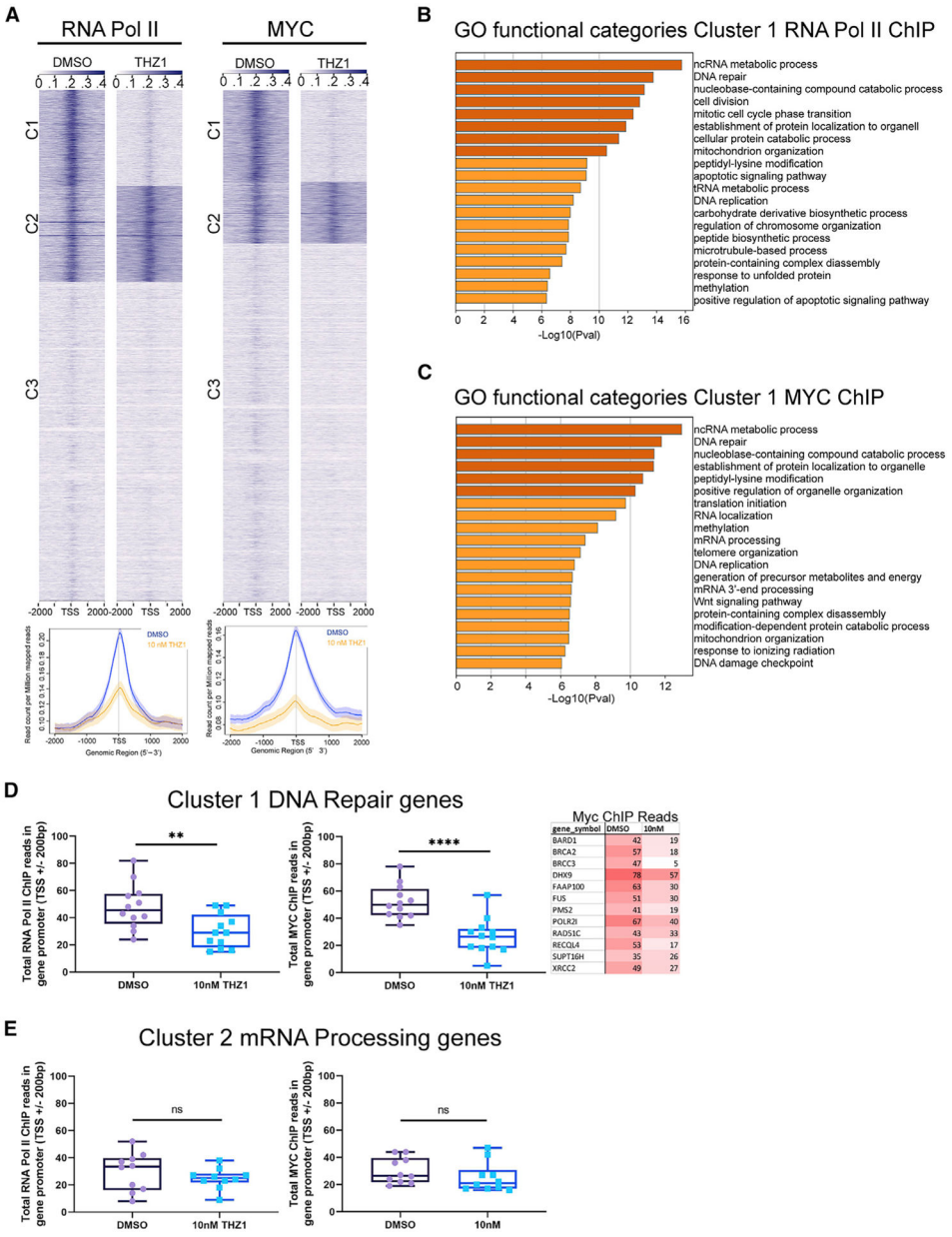

Figure 5. CDK7 inhibition abrogates RNA Pol II and MYC promoter association

(A) ChIP sequencing with RNA Pol II and MYC antibody performed on D458 cells treated with DMSO versus 10 nM THZ1. Heatmap of normalized RNA Pol II or MYC at the TSS. (Bottom) average read density of RNA Pol II or MYC ChIP sequencing at the TSS. DMSO (blue) or 10 nM THZ1 (yellow).

(B) GO functional categories for RNA Pol II ChIP cluster 1 genes affected by THZ1 treatment. Enrichment scores are shown as −log10(Pval).

(C) GO functional categories for MYC ChIP cluster 1 genes affected by THZ1 treatment. Enrichment scores are shown as −log10(Pval).

(D) Box-and-whisker plots ± min and max of the total number of reads within 200 bp of the TSS for the top genes within the DNA Repair ontology of cluster 1 for RNA Pol II ChIP and

MYC ChIP. MYC ChIP read numbers for top DNA repair genes (right). Statistical analysis, two-tailed, unpaired t test. ****$p < 0.0001$; **$p < 0.01$. Color scale indicates high (red) to low (white) reads.

(E) Top genes within the mRNA processing ontology of cluster 2 for RNA Pol II and MYC ChIPs. Statistical analysis, two-tailed, unpaired t test. ns, not significant.

See also Figure S5.

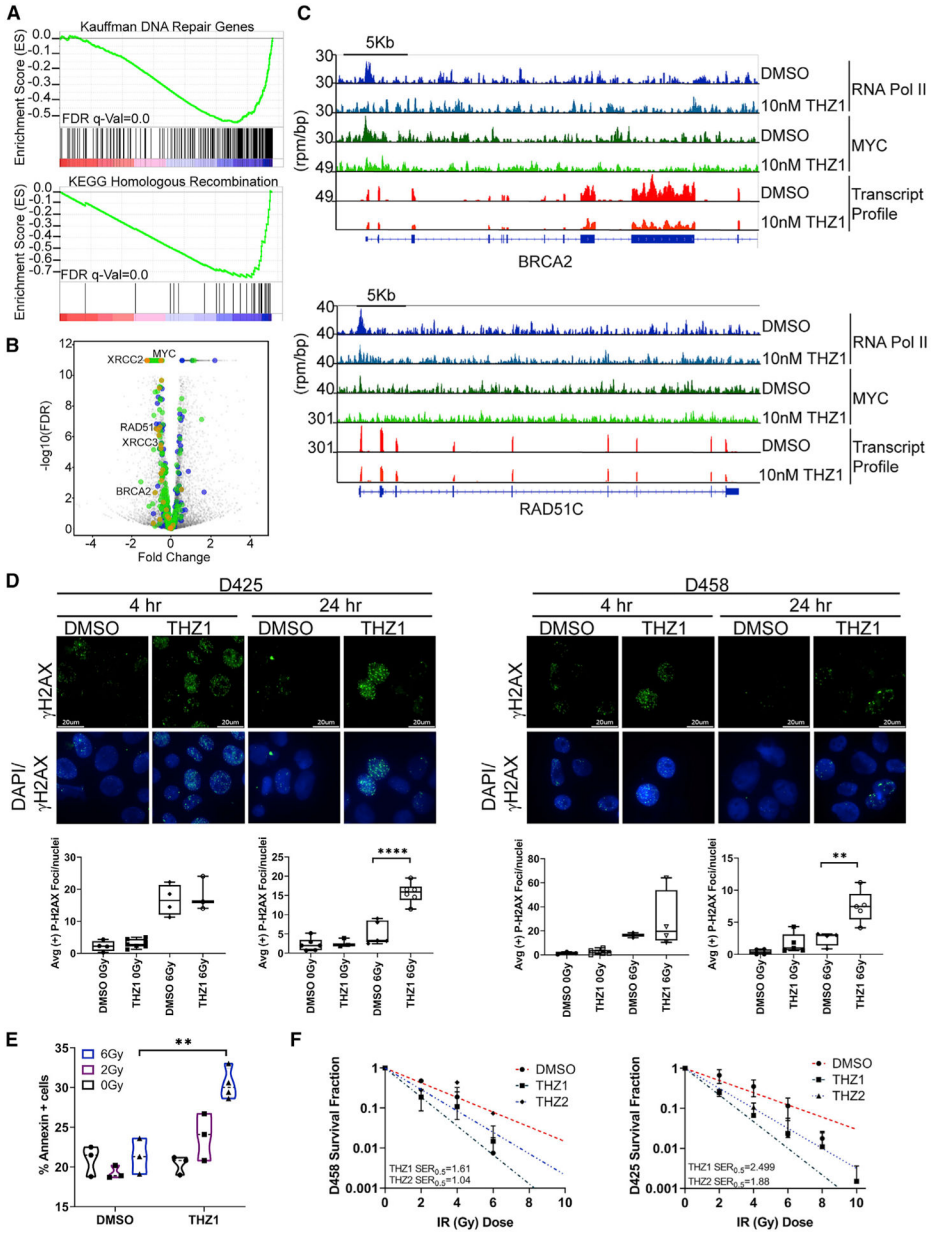

Figure 6. CDK7 inhibition minimizes DNA damage response enhancing susceptibility to IR

(A) GSEA from THZ1 D458 treatment RNA-seq. Kauffman DNA repair, KEGG homologous recombination. FDR q value = 0.0.

(B) Volcano plot of Kauffman DNA repair (green), KEGG homologous recombination (yellow), and MYC targets (blue) from THZ1-treated D458 cells.

(C) Individual ChIP gene tracks of RNA Pol II, MYC signals, and RNA transcript profile for DMSO and THZ1 10-nM D458 treatments. Shown are the y axis signal density (rpm/bp) of BRCA2 promoter and RAD51C promoter.

(D) Immunofluorescence of γH2AX (green) and DAPI at 6 Gy. Scale bar, 20 μm. (below) Quantification, box-and-whisker plots ± min and max of γH2AX foci/nuclei. n = 4/treatment group. Statistical analysis, one-way ANOVA, ****$p < 0.0001$; **$p < 0.001$.

(E) Annexin V (+) staining assay. D458 cells treated with DMSO or THZ1 200 pM and IR at 0, 2, and 6 Gy. Violin plot of the percentage of Annexin V (+) stained cells (y axis) is shown. n = 3. Statistical analysis, two-way ANOVA. **p < 0.005.

(F) Survival fraction plots of D458 and D425 from cells treated with DMSO or THZ1/2 200 pM and increasing IR 0, 2, 4, 6, 8, 10 Gy. n = 3. Survival fraction (y axis) mean ± SD versus IR (x axis). Survival enhancement ratio is shown for THZ1 and THZ2.

See also Figures S2 and S6.

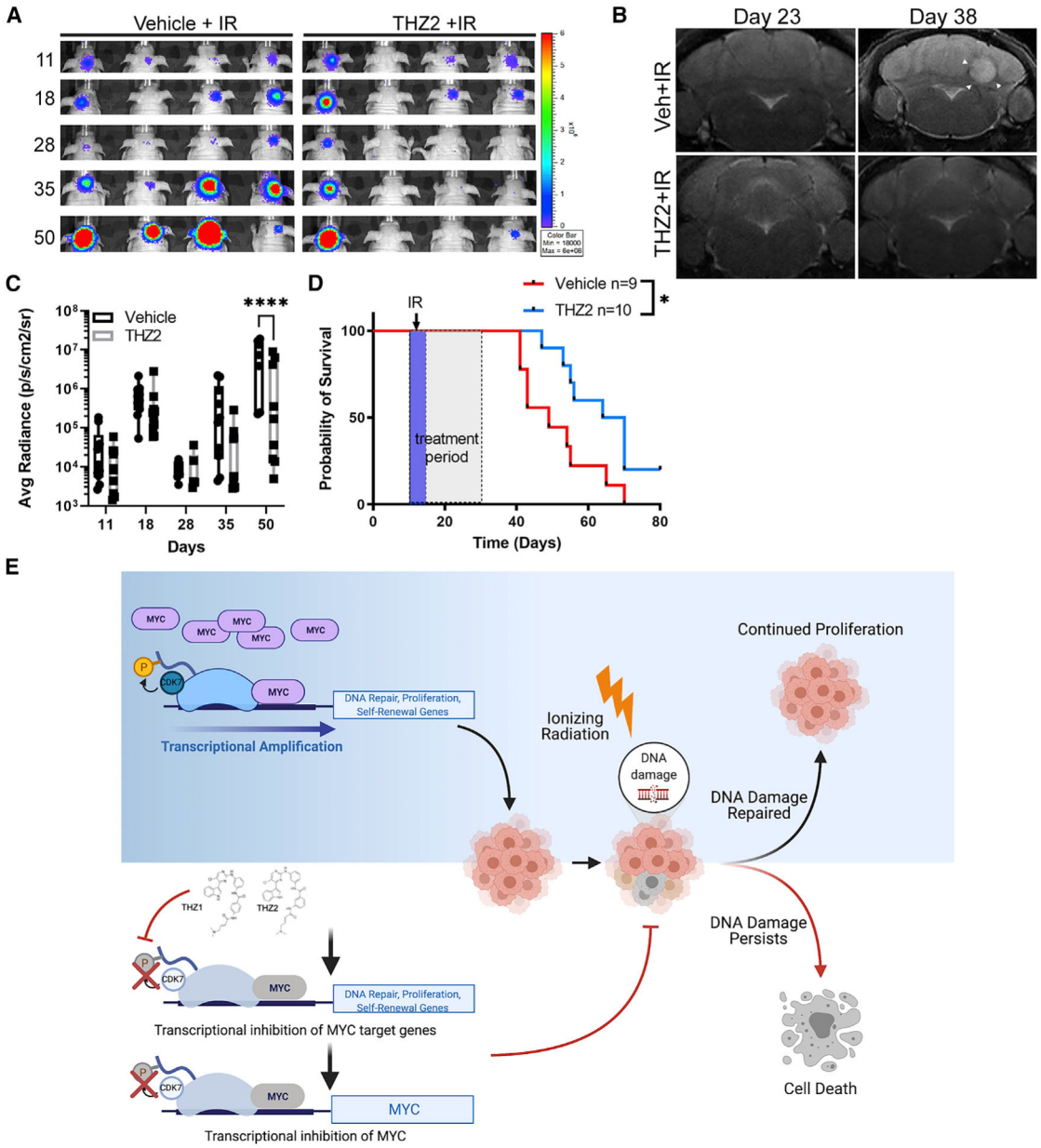

Figure 7. ***In vivo*** **IR with CDK7 inhibition**

(A) Representative bioluminescence images of xenograft D458 vehicle or THZ2 15 mg/kg treated with 1.5 Gy over 5 days starting at day 15 post-injection. Color scales indicate bioluminescence radiance in photons/sec/cm^2/steradian.

(B) Representative MRI of vehicle + IR and THZ2 + IR treated D458 xenograft mice at 23 and 49 days. White arrows indicate tumor.

(C) Box-and-whisker plot ± min and max of mean total radiance in photons/sec/cm^2/steradian. Statistical analysis, two-way ANOVA, ****$p < 0.0001$.

(D) Kaplan-Meier survival curve of D458 xenograft mice treated with vehicle (n = 9) or THZ2 (n = 10) and 1.5 Gy for 5 days (violet box). THZ2 treatment period for 25 days, shaded box. Statistical analysis, log-rank (Mantel-Cox) test, *$p < 0.05$.

(E) MYC gene amplification in group 3 MB drives highly active transcription of DNA repair, proliferation, and self-renewal genes shielding cells against IR and sustaining growth. Treatment with THZ1/THZ2 blocks RNA Pol II association at the MYC promoter, limiting MYC transcription, and blocks RNA Pol II and MYC association with select gene promoters, removing MB tumor cells' defense mechanisms and leading to cell death. Image created with BioRender.com.

KEY RESOURCES TABLE

REAGENT or RESOURCE	SOURCE	IDENTIFIER
Antibodies		
Rabbit monoclonal Phospho-Rpb1 CTD (Ser5)	Cell Signaling	Cat#13523;RRID:AB_2798246
Rabbit monoclonal Phospho-Rpb1 CTD (Ser2)	Cell Signaling	Cat#13499;RRID:AB_2798238
Mouse monoclonal CDK7	Cell Signaling	Cat#2916;RRID:AB_2077142
Rabbit monoclonal CDK9	Cell Signaling	Cat#2316;RRID:AB_2291505
Rabbit polyclonal PARP/cleaved PARP	Cell Signaling	Cat#9542;RRID:AB_2160739
Rabbit monoclonal cMYC	Cell Signaling	Cat#5605;RRID:AB_1903938
Rabbit polyclonal RNA Pol II	Bethyl Laboratories	Cat#A300–653A; RRID:AB_519334
Anti-Mouse IgG-HRP linked	Cell Signaling	Cat#7076;RRID:AB_330924
Anti-Rabbit IgG-HRP linked	Cell Signaling	Cat#7074;RRID:AB_2099233
Mouse monoclonal β-Actin-HRP linked	Cell Signaling	Cat#12262;RRID:AB_2566811
Rabbit monoclonal Phospho-Histone H2A.X (Ser139)	Cell Signaling	Cat#9718;RRID:AB_2118009
Rabbit polyclonal RPA70/RPA1	Cell Signaling	Cat#2267;RRID:AB_2180506
Rabbit monoclonal Ki67	Thermo Fisher Scientific	Cat#RM-9106; RRID:AB_2335745
Mouse monoclonal RAD51	Novus Biologicals	Cat#NB100–148; RRID:AB_10002131
Rabbit polyclonal Cleaved Caspase 3	Cell Signaling	Cat#9661:RRID:AB_2341188
Rabbit monoclonal RNA Polymerase II CTD	abCAM	Cat#ab817; RRID:AB_306327
Rabbit monoclonal cMYC	Cell signaling	Cat#13987;RRID:AB_2631168
Goat Anti-Rabbit IgG (H+L) Polyclonal Antibody, Alexa Fluor 488 Conjugated	Thermo Fisher Scientific	Cat#A-11008; RRID:AB_143165
Goat Anti-Rabbit IgG (H+L) Polyclonal Antibody, Alexa Fluor 555 Conjugated	Thermo Fisher Scientific	Cat# A-31572; RRID:AB_162543
Biological samples		
Normal Cerebellum paraffin blocks	Dr. Nicholas Foreman lab	N/A
Patient embedded tumor paraffin blocks	Dr. Nicholas Foreman lab	N/A
Chemicals, peptides, and recombinant proteins		
THZ1	Cayman Chemical	Cat#9002215
THZ2	MedChem Express	Cat#HY-12280/CS-3245
YKL-5–124	Selleckchem	Cat#S8863
CT7001	MedChem Express	Cat#HY-103712A
Nitrotetrazolium blue chloride	Sigma Aldrich	Cat# N6876–50MG
Critical commercial assays		
Guava Nexin Assay	Millipore	Cat#4500–0450
CellTiter 96 Aqueous One Solution Cell Proliferation	Promega	Cat#G3580
RNeasy Mini Kit	QIAGEN	Cat#74104
DNeasy Blood and Tissue Kit	QIAGEN	Cat#69504

REAGENT or RESOURCE	SOURCE	IDENTIFIER
High Capacity Reverse Transcription Kit	Thermo Fisher Scientific	Cat#4368814
TaqMan Universal Master Mix II, no UNG	Thermo Fisher Scientific	Cat#4400040
Venor GeM Mycoplasma Detection Kit	Sigma Aldrich	Cat#MP0025–1kt
Qubit dsDNA High Sensitivity Assay	Thermo Fisher Scientific	Cat#Q32851
Lipofectamine 3000 Transfection Reagent	Thermo Fisher Scientific	Cat#L3000008
Ovation UltraLow system V2	Nugen	Cat#0344
Deposited data		
ChIP sequencing	This paper	https://www.ncbi.nlm.nih.gov/geo/query/acc.cgi?acc=GSE164696
Expression profile high throughput sequencing THZ1 treatment	This paper	https://www.ncbi.nlm.nih.gov/geo/query/acc.cgi?acc=GSE164933
Expression profile high throughput sequencing shCDK7 Raw data	This paper	https://www.ncbi.nlm.nih.gov/geo/query/acc.cgi?acc=GSE164933
CDK7 full Western Blots	This paper	http://data.mendeley.com/login?redirectPath=/datasets/x6nzmgx97h/draft?a=666c232d-8dd5-4046-8faa-f28109c48a4c
Experimental models: Cell lines		
D458	Dr. Darell Bigner lab	Gift;RRID:CVCL_1161
D425	Dr. Darell Bigner lab	Gift;RRID:CVCL_1275
D283	ATCC	Cat#ATCC-HTB-185;RRID:CVCL_1155
DAOY	ATCC	Cat#ATCC-HTB-186;RRID:CVCL_1167
UW228	Dr. John Silber lab	Gift;RRID:CVCL_4460
ONS76	Dr. James Rutka lab	Gift;RRID:CVCL_1624
ONS76-RFP	Dr. James Rutka lab; Moreira et al., 2020	RRID:CVCL_1624
ONS76-MYC	Dr. James Rutka lab; Moreira et al., 2020	RRID:CVCL_1624
MED411FH	Cook Sangar et al., 2017	N/A
RPE-Neo	Dr. Andre Goga lab	Gift;RRID:CVCL_GQ00
RPE-MYC	Dr. Andre Goga lab	Gift;RRID:CVCL_GQ00
NIH 3T3	Dr. John Silber lab	Gift;RRID:CVCL_0594

REAGENT or RESOURCE	SOURCE	IDENTIFIER
NHA	Dr. Cynthia Hawkins lab	Gift
HEK293FT	ATCC	Cat#PTA-5077; RRID:CVCL_6911
Experimental models: Organisms/strains		
Athymic Nude-Foxn1^{nu} mice	The Jackson Laboratory	Cat#07850
NSG, NOD scid gamma	The Jackson Laboratory	Cat#005557
Oligonucleotides		
TaqMan Probe CDK7 Hs00361486_m1	Thermo Fisher Scientific	Cat#4331182
TaqMan Probe BRCA2 Hs00609073_m1	Thermo Fisher Scientific	Cat#4331182
TaqMan Probe RAD51 Hs00947967_m1	Thermo Fisher Scientific	Cat#4331182
TaqMan Probe Gapdh Hs02786624_g1	Thermo Fisher Scientific	Cat#4331182
Recombinant DNA		
Mission shRNA CDK7; **Sequence**:CCGGGTGGGCTGTTGGCTGTATATTCTCGAGAATATACAGCCAACAGCCCACTTTTT	Sigma Aldrich	Cat#TRCN0000000595
Mission shRNA CDK7; **Sequence**:CCGGGCTGTAGAAGTGAGTTTGTAACTCGAGTTACAAACTCACTTCTACAGCTTTTT	Sigma Aldrich	Cat#TRCN0000000592
Mission shRNA CDK7; **Sequence**:CCGGGAAACTGATCTAGAGGTTATACTCGAGTATAACCTCTAGATCAGTTTCTTTTTG	Sigma Aldrich	Cat#TRCN0000230910
Mission pLKO.1-puro non-target shRNA control plasmid	Sigma Aldrich	Cat#SHC016
LentiCRISPRv2	Addgene	Cat#52961
LentiGUIDE-puro	Addgene	Cat#52963
pMD2.G	Addgene	Cat#12259
psPAX2	Addgene	Cat#12260
Software and algorithms		
DESeq2 R package	Love et al., 2014	10.18129/B9.bioc.DESeq2
Bowtie v2	Langmead et al., 2009	http://bowtie-bio.sourceforge.net/index.shtml
Samtools version 1.5	Li et al., 2009	https://github.com/samtools/samtools
MACs2 (v2.1.1.20160309	Zhang et al., 2008	https://github.com/macs3-project/MACS/releases
ChIPseeker	Yu et al., 2015	N/A
IGV v.2.3.82	Thorvaldsdóttir et al., 2013	http://software.broadinstitute.org/software/igv/
Metascape	Zhou et al., 2019	http://metascape.org/gp/index.html
MSigDB	Subramanian et al., 2005	https://www.gsea-msigdb.org/gsea/index.jsp
ImageJ	Schneider et al., 2012	https://imagej.nih.gov/ij/download.html
Living Image v2.60.1	Perkin Elmer	N/A

REAGENT or RESOURCE	SOURCE	IDENTIFIER
ParaVision Neo	Bruker	N/A
Graphpad Prism 9	Graphpad	N/A
DAVID Bioinformatics database	Huang et al., 2009a, 2009b	https://david.ncifcrf.gov/